

# SCALABLE PRECONDITIONERS FOR THE PSEUDO-4D DFN LITHIUM-ION BATTERY MODEL\*

THOMAS ROY<sup>†</sup>, NICHOLAS W. BRADY<sup>†</sup>, GIOVANNA BUCCI<sup>†</sup>, NICHOLAS R. CROSS<sup>†</sup>, VICTORIA M. EHLINGER<sup>†</sup>, TIRAS Y. LIN<sup>†</sup>, HANYU LI<sup>†</sup>, AND MARCUS A. WORSLEY<sup>†</sup>

**Abstract.** The pseudo-4D Doyle–Fuller–Newman (DFN) model enables predictive simulation of lithium-ion batteries with three-dimensional electrode architectures and particle-scale diffusion, extending the standard pseudo-2D (P2D) formulation to fully resolve cell geometry. This leads to large, nonlinear systems with strong coupling across multiple physical scales, posing significant challenges for scalable numerical solution. We introduce block-structured preconditioning strategies that exploit the mathematical properties of the coupled system, employing multigrid techniques for electrode-level operators and localized solvers for particle-scale diffusion. Comprehensive scalability studies are performed across a range of geometries, including homogeneous and heterogeneous cubic cells, flattened jelly-roll configurations, and triply periodic minimal surface electrodes, to assess solver robustness and parallel scalability. The proposed methods consistently deliver efficient convergence and enable the solution of battery models with hundreds of millions of degrees of freedom on large-scale parallel hardware.

**Key words.** block preconditioning, battery simulation, finite element method, Doyle–Fuller–Newman model, multi-scale modeling, high-performance computing

**MSC codes.** 65N30, 65F08, 65Y05, 65M60

**1. Introduction.** Lithium-ion batteries are ubiquitous, with applications spanning consumer electronics, electric vehicles, and grid-scale energy storage systems. Predictive, physics-based simulation is essential for the design, safety, and optimization of these devices [12]. Among continuum-scale models for full battery cells, the Doyle–Fuller–Newman (DFN) model is a widely accepted standard [22, 25].

The classical DFN model is often referred to as a pseudo-two-dimensional (P2D) formulation, as it couples one-dimensional through-cell transport with radial diffusion in spherical active-material particles, thereby capturing essential multiscale physics at manageable computational cost. These assumptions are well suited to layered, homogeneous, slab-like electrodes, for which spatial variations are predominantly through the cell thickness and the geometry can be modeled effectively in one dimension. However, many modern battery architectures increasingly violate this one-dimensional geometric assumption [33, 42, 17].

Commercial batteries are commonly manufactured as prismatic or cylindrical cells composed of thin electrodes that are stacked and rolled. As a first approximation, P2D models are typically employed for such cells, neglecting variations along the length of the electrodes. Nevertheless, tab placement and current-collector geometry can induce pronounced three-dimensional variations in electrochemical response [52, 57]. In addition, certain forms of microstructural heterogeneity can be incorporated into continuum-scale simulations [43, 47]. These conventional slab-like electrode geometries arise from traditional manufacturing techniques, while advanced manufacturing approaches enable new electrode architectures and increased thick-

---

\* Uploaded on February 6, 2026.

**Funding:** This work was performed under the auspices of the U.S. Department of Energy by Lawrence Livermore National Laboratory under Contract DE-AC52-07NA27344. This work was supported by the Lawrence Livermore National Laboratory LDRD 23-SI-002. LLNL release number: LLNL-JRNL-2015625-DRAFT.

<sup>†</sup>Lawrence Livermore National Laboratory, Livermore, CA, United States of America. Corresponding author: Thomas Roy (roy27@llnl.gov).

nesses [64, 9, 67, 65, 61, 58]. Such structured electrodes naturally introduce nontrivial three-dimensional spatial variations in transport and reaction processes. Moreover, additional physical mechanisms, including thermal transport and mechanical stress due to swelling, act across the full three-dimensional cell geometry and across electronically insulating layers [40, 34, 39, 14]. Similarly, electrolyte motion induced by electrode deformation is an increasingly studied phenomenon that can significantly impact performance and degradation in commercial cells [2, 10].

Several recent studies have extended the classical DFN equations to fully three-dimensional geometries while retaining radial particle-scale diffusion, yielding pseudo-four-dimensional (P4D) formulations that resolve geometric heterogeneity and multi-physics effects inaccessible to one-dimensional through-cell models. At the cell scale, P4D electrochemical-thermal formulations for layered geometries have been implemented in commercial multiphysics software, including COMSOL Multiphysics® [20, 38, 42, 15]. To reduce the cost of resolving repeated layered structures, reduced-order P4D frameworks have been introduced in Abaqus®, preserving three-dimensional resolution [28, 19]. At the electrode-architecture scale, P4D formulations have been employed to study explicitly resolved three-dimensional porous and additively manufactured geometries, including lattices, fins, and TPMS-based structures, using COMSOL and the open-source code Firedrake [27, 17, 29]. Beyond electrochemical-thermal coupling, strongly coupled P4D frameworks incorporating mechanics, heat transport, and porous electrolyte flow have been proposed in Abaqus® for fully three-dimensional cell geometries [35]. P4D formulations have also been combined with operando measurements to resolve depth-dependent lithiation heterogeneity in structured electrodes [60]. In contrast to this predominantly application-driven literature, Xu and Cao analyzed the numerical structure of the P4D DFN equations and established optimal finite element convergence rates in spatial dimensions greater than one [63]. Nearly all existing P4D studies rely on direct solvers, which fundamentally limits problem size and restricts physical fidelity to small-scale demonstrations with fewer than  $10^5$  mesh elements. To our knowledge, the only work employing a scalable solver is [17], which represents prior work by the present authors.

The P4D model gives rise to tightly coupled nonlinear systems that can become extremely large. Electrolyte concentration, ionic potential, electronic potential, and solid-phase concentration are strongly coupled through nonlinear charge-transfer reactions within the electrodes. This strong coupling, combined with a wide range of characteristic time scales, limits the effectiveness of segregated solution strategies, which typically require prohibitively small time steps; fully coupled implicit approaches are therefore preferred. This limitation was recognized early in the context of pseudo-2D models, where a direct solver, referred to as `BAND(J)`, exploited the banded structure of the resulting linear systems [45, 46]. For pseudo-4D models, however, direct solvers do not scale with the size of the electrode-level system, which arises from the discretization of three-dimensional differential operators. Scalable solution strategies for such systems therefore require iterative methods equipped with effective preconditioning strategies [59].

A natural approach for solving the coupled nonlinear systems arising from fully implicit time discretization is Newton's method combined with a Krylov subspace method for the linearized systems. The efficiency of this approach critically depends on the availability of robust and scalable preconditioners. Naive application of incomplete factorization or monolithic multigrid methods typically fails or exhibits poor scalability. Fortunately, the DFN system exhibits a rich block structure that can be exploited in the design of effective preconditioners. Several preconditioning strategies

have been proposed for battery simulations that neglect particle-scale diffusion, often in the context of explicitly resolving electrode microstructures [62, 3, 24].

In this work, we present scalable preconditioners for the fully implicit solution of the pseudo-4D DFN model in three-dimensional cell geometries, and demonstrate both strong and weak scaling with respect to refinement of the three-dimensional electrode mesh. We consider block preconditioners that exploit the intrinsic structure of the coupled system and the mathematical properties of its constituent blocks. The electrode-level blocks correspond to elliptic or parabolic operators and are therefore well suited to multigrid methods [11]. In contrast, the particle-level block consists of many small, local systems that can be addressed efficiently using localized solution strategies. Both block-diagonal and block-triangular preconditioning approaches are examined, allowing for a trade-off between computational cost and fidelity of inter-equation coupling. These preconditioning strategies enable the solution of large-scale, fully coupled three-dimensional battery simulations with over  $10^7$  mesh elements.

In section 2, we describe the pseudo-4D DFN model for three-dimensional cell geometries. In section 3, we describe the spatial and temporal discretizations, using finite elements for the electrode-level equations and finite differences in spherical coordinates for the particle-scale diffusion equations, with fully coupled implicit time-stepping. In section 4, we analyze the resulting block system and introduce the proposed preconditioning strategies. Finally, in section 5, we present four test cases and perform scalability studies for large-scale problems.

**2. Governing equations.** We consider the Doyle–Fuller–Newman (DFN) model for lithium-ion batteries [22, 25], generalized to cells with three-dimensional geometries of arbitrary shape. The domain  $\Omega \subset \mathbb{R}^3$  is partitioned into negative electrode (anode)  $\Omega_n$ , separator (membrane)  $\Omega_m$ , and positive electrode (cathode)  $\Omega_p$ , such that  $\Omega = \Omega_n \cup \Omega_m \cup \Omega_p$  and these subdomains are disjoint. By convention, electrode signs in batteries are defined according to their polarity during discharge, when the cell delivers power. Each point  $\mathbf{x} \in \Omega_n \cup \Omega_p$  is associated with a representative spherical active material particle of radius  $R_s(\mathbf{x})$ . Here we assume  $R_s = R_p$  in  $\Omega_p$  and  $R_s = R_n$  in  $\Omega_n$ , where both  $R_p$  and  $R_n$  are constant values associated with the active material in their respective electrode. This corresponds to a homogenized description in which particle size distributions are approximated by representative mean values. The electrode-scale and particle-scale domains are coupled through charge-transfer reactions occurring throughout the electrodes and at particle surfaces, as detailed below, yielding the pseudo-4D model illustrated in Figure 1. Parameter values for the following equations are given in Appendix C for the test cases considered in section 5.

**2.1. Lithium diffusion in active particles.** The solid-phase lithium concentration  $c_s = c_s(r, \mathbf{x}, t)$  in the particle satisfies

$$(2.1) \quad \frac{\partial c_s}{\partial t} = \frac{1}{r^2} \frac{\partial}{\partial r} \left( D_s r^2 \frac{\partial c_s}{\partial r} \right), \quad r \in [0, R_s(\mathbf{x})],$$

where  $D_s$  is the solid-phase diffusivity. At the particle center, symmetry requires

$$(2.2) \quad \left. \frac{\partial c_s}{\partial r} \right|_{r=0} = 0.$$

At the surface, the radial flux is proportional to the reaction current density  $i_n$ ,

$$(2.3) \quad -D_s \left. \frac{\partial c_s}{\partial r} \right|_{r=R_s} = \frac{i_n}{F},$$

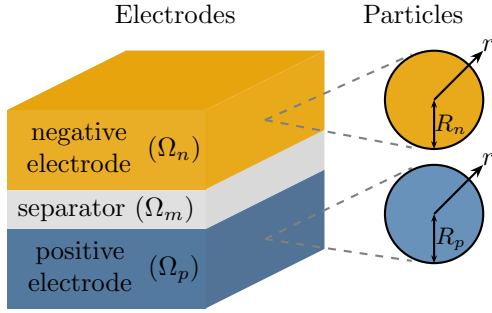


Fig. 1: Schematic of the pseudo-4D DFN battery model with 3D electrodes and 1D spherical particles.

where  $F$  is Faraday's constant.

**2.2. Electrolyte transport.** The electrolyte-phase lithium concentration  $c_e = c_e(\mathbf{x}, t)$  satisfies the conservation equation

$$(2.4) \quad \varepsilon \frac{\partial c_e}{\partial t} - \nabla \cdot (D_e^{\text{eff}} \nabla c_e) = \frac{1 - t_+^0}{F} a i_n, \quad \text{in } \Omega,$$

where  $\varepsilon(\mathbf{x})$  is the local porosity,  $t_+^0$  is the transference number, and  $a(\mathbf{x})$  is the electrochemically active surface area per volume ratio. The transference number may in general depend on the electrolyte concentration  $c_e$  [22]; here it is taken to be constant, consistent with the material parameters specified in Appendix C. The effective diffusivity is given by the Bruggeman correlation [13]

$$(2.5) \quad D_e^{\text{eff}}(\mathbf{x}, c_e) = \varepsilon(\mathbf{x})^b D_e(c_e),$$

where  $D_e(c_e)$  is the bulk electrolyte diffusivity and  $b = 1.5$  is the Bruggeman exponent.

**2.3. Charge conservation.** The electrolyte-phase (ionic) potential,  $\phi_e = \phi_e(\mathbf{x}, t)$  satisfies

$$(2.6) \quad -\nabla \cdot \left( \kappa^{\text{eff}} \nabla \phi_e + \kappa^{\text{eff}} \frac{2RT(1 - t_+^0)}{Fc_e} \nabla c_e \right) = a i_n, \quad \text{in } \Omega.$$

The effective electrolyte conductivity is defined as

$$(2.7) \quad \kappa^{\text{eff}}(\mathbf{x}, c_e) = \varepsilon(\mathbf{x})^b \kappa(c_e),$$

where  $\kappa(c_e)$  is the bulk electrolyte conductivity.

The solid-phase (electronic) potential  $\phi_s = \phi_s(\mathbf{x}, t)$  is defined in the electrode domains and satisfies

$$(2.8) \quad -\nabla \cdot (\sigma^{\text{eff}} \nabla \phi_s) = -a i_n, \quad \text{in } \Omega_n \cup \Omega_p.$$

The effective solid-phase conductivity accounts for the active material phase volume fraction  $\varepsilon_s(\mathbf{x})$ , and is given by

$$(2.9) \quad \sigma^{\text{eff}}(\mathbf{x}) = \varepsilon_s(\mathbf{x})^b \sigma,$$

where  $\sigma$  is the bulk conductivity of the active material.

**2.4. Interfacial kinetics.** The interfacial reaction current density  $i_n$  follows the Butler–Volmer relation in exponential form:

$$(2.10) \quad i_n = i_0 \left[ \exp \left( \frac{\alpha_a F}{RT} \eta \right) - \exp \left( -\frac{\alpha_c F}{RT} \eta \right) \right],$$

where  $\eta = \phi_s - \phi_e - U_{\text{ocp}}(c_s^{\text{surf}})$  is the overpotential,  $R$  is the universal gas constant, and  $T$  is the temperature. Here,  $\alpha_a$  and  $\alpha_c$  are the anodic and cathodic charge-transfer coefficients ( $\alpha_a + \alpha_c = 1$ ), and  $c_s^{\text{surf}} = c_s(R_s(\mathbf{x}), \mathbf{x}, t)$  is the surface concentration of the active particle. The exchange current density  $i_0$  depends on both the electrolyte and solid-phase concentrations, typically modeled as

$$(2.11) \quad i_0 = k c_e^{\alpha_a} (c_{s,\text{max}} - c_s^{\text{surf}})^{\alpha_a} (c_s^{\text{surf}})^{\alpha_c},$$

where  $k$  is a rate constant and  $c_{s,\text{max}}$  is the maximum lithium concentration in the solid.

**2.5. Boundary and initial conditions.** Boundary conditions are imposed on  $\partial\Omega$  to model current collectors, insulation, and symmetry, depending on the physical configuration. In this work, we will consider applied current boundary conditions (as opposed to applied voltage). Thus, at the positive current collector, a Neumann condition is applied to  $\phi_s$  to enforce the applied current density such that

$$(2.12) \quad \sigma^{\text{eff}} \nabla \phi_s \cdot \mathbf{n} = \frac{I_{\text{app}}}{A}, \quad \text{on } \Gamma_p$$

where  $I_{\text{app}}$  is the applied current and  $A$  is the area of the positive current collector  $\Gamma_p$ . At the negative current collector  $\Gamma_n$ , the solid potential is grounded via a Dirichlet boundary condition:

$$(2.13) \quad \phi_s = 0, \quad \text{on } \Gamma_n.$$

At the interfaces between the electrodes ( $\Omega_n, \Omega_p$ ) and the separator ( $\Omega_m$ ), a zero-flux (Neumann) boundary condition is imposed on  $\phi_s$ . The electrolyte phase ( $\phi_e, c_e$ ) is subject to zero-flux conditions on insulating boundaries (the exterior boundary of  $\Omega$ ). Initial conditions must be provided for  $c_e(\mathbf{x}, 0)$ ,  $\phi_e(\mathbf{x}, 0)$ ,  $\phi_s(\mathbf{x}, 0)$ , and  $c_s(r, \mathbf{x}, 0)$ .

**3. Discretization.** In this section, we introduce our discretization scheme including a finite difference scheme for the particle equation and a finite element discretization for the electrode-level equations. We also note details related to implementing the coupled scheme in a finite element framework.

**3.1. Spatial discretization of the particle equation.** We discretize the radial diffusion equation (2.1) for the solid-phase concentration,  $c_s(r)$ , in spherical active material particles using a finite difference method on a one-dimensional, nonuniform spherical mesh. The scheme combines the scheme for spherical coordinates from [56] and the scheme for nonuniform meshes from [55].

Let  $\{r_i\}_{i=1}^{N_c}$  denote a strictly increasing sequence of radial node locations such that  $r_1 = 0$  and  $r_{N_c} = R_s$ , defining the computational mesh. We define  $\Delta r_{i-1} = r_i - r_{i-1}$ ,  $\Delta r_i = r_{i+1} - r_i$ , and the local mesh ratio  $\theta_i = \Delta r_i / \Delta r_{i-1}$ .

The differential operator in (2.1) is written as a sum of two terms:

$$(3.1) \quad \frac{1}{r^2} \frac{d}{dr} \left( r^2 \frac{dc_s}{dr} \right) = \frac{2}{r} \frac{dc_s}{dr} + \frac{d^2 c_s}{dr^2},$$

each of which is approximated separately.

For interior nodes  $2 \leq i \leq N_c - 1$ , we discretize the first derivative and second derivative terms as

$$(3.2) \quad \mathcal{L}_1(c)_i = \frac{2D_s}{r_i} \frac{c_{i+1} - \theta_i^2 c_{i-1} - (1 - \theta_i^2) c_i}{\Delta r_i (1 + \theta_i)},$$

$$(3.3) \quad \mathcal{L}_2(c)_i = D_s \frac{2}{\Delta r_i \Delta r_{i-1} (1 + \theta_i)} (c_{i+1} + \theta_i c_{i-1} - (1 + \theta_i) c_i).$$

The full discrete Laplacian at node  $i$  is given by

$$(3.4) \quad \mathcal{L}_h(c)_i = \mathcal{L}_1(c)_i + \mathcal{L}_2(c)_i.$$

The zero-flux boundary condition at the particle center (2.2) is discretized using a second-order one-sided approximation:

$$(3.5) \quad \mathcal{L}_h(c)_1 = \frac{6D_s}{\Delta r_1^2} (c_2 - c_1).$$

At the particle surface, the flux boundary condition (2.3) is enforced using a second-order backward difference:

$$(3.6) \quad \mathcal{L}_h(c)_{N_c} = \frac{2D_s}{\Delta r_{N_c-1}^2} (c_{N_c-1} - c_{N_c}) + \frac{2i_n}{F \Delta r_{N_c-1}} \left( 1 + \frac{\Delta r_{N_c-1}}{R_s} \right).$$

The spatially discretized particle system is thus given by

$$(3.7) \quad \frac{\partial c_{s,i}}{\partial t} = \mathcal{L}_h(c_s)_i, \quad \text{for } i = 1, \dots, N_c,$$

where  $c_{s,i} \approx c_s(r_i)$ .

*Remark 3.1.* From [55], the spatial discretization described above is second-order accurate in space, provided the mesh is locally regular. Specifically, if adjacent cells satisfy  $\Delta r_i - \Delta r_{i-1} = \mathcal{O}(\Delta r_{i-1}^2)$  or  $\mathcal{O}(\Delta r_i^2)$ , then the local truncation error is  $\mathcal{O}(\Delta r_{i-1}^2)$  at all nodes. If this condition is violated (e.g., under strongly graded meshes), the scheme remains consistent but only achieves first-order spatial accuracy.

For this study, we choose a regular mesh defined using a geometric progression. Let the ratio between the first and last element  $\bar{\theta} = \Delta r_1 / \Delta r_{N_c-1}$ , where  $0 < \bar{\theta} < 1$ . The elements get progressively smaller using the relationship

$$(3.8) \quad \Delta r_i = \bar{\theta}^{\frac{1}{N_c-2}} \Delta r_{i-1}.$$

This exponentially smooth mesh is more regular than the regularity required in Remark 3.1.

**3.2. Spatial discretization for the electrode-level equations.** The three-dimensional equations for the electrolyte concentration  $c_e$ , electrolyte potential  $\phi_e$ , and solid potential  $\phi_s$  are discretized using continuous, piecewise linear finite elements on a conforming tetrahedral or hexahedral mesh of the domain  $\Omega$ . Let  $V_h \subset H^1(\Omega)$  denote the standard finite element space of continuous, piecewise linear functions, and

$V_h^0 = \{v \in V_h \mid v = 0 \text{ on } \Gamma_n\}$ , i.e. to strongly enforce the ground boundary condition (2.13).

The governing equations are coupled through the reaction current density  $i_n$ , which depends on the solution of the particle-level diffusion equation at each point in the electrodes. We adopt a monolithic approach in which all variables including the particle concentrations are solved simultaneously as part of a single nonlinear system. Here we write the variational formulation for the electrode-level equations.

We seek  $c_e, \phi_e \in V_h$  and  $\phi_s \in V_h^0$  such that the following variational equations are satisfied for all test functions  $v_{c_e}, v_{\phi_e} \in V_h$  and  $v_{\phi_s} \in V_h^0$ , respectively:

$$(3.9) \quad \int_{\Omega} \varepsilon \frac{\partial c_e}{\partial t} v_{c_e} \, d\mathbf{x} + \int_{\Omega} D_e^{\text{eff}} \nabla c_e \cdot \nabla v_{c_e} \, d\mathbf{x} = \int_{\Omega} \frac{1 - t_+^0}{F} a i_n v_{c_e} \, d\mathbf{x},$$

$$(3.10) \quad \int_{\Omega} \kappa^{\text{eff}} \nabla \phi_e \cdot \nabla v_{\phi_e} \, d\mathbf{x} + \int_{\Omega} \kappa^{\text{eff}} \frac{2RT(1 - t_+^0)}{Fc_e} \nabla c_e \cdot \nabla v_{\phi_e} \, d\mathbf{x} = \int_{\Omega} a i_n v_{\phi_e} \, d\mathbf{x},$$

$$(3.11) \quad \int_{\Omega_n \cup \Omega_p} \sigma^{\text{eff}} \nabla \phi_s \cdot \nabla v_{\phi_s} \, d\mathbf{x} = - \int_{\Omega_n \cup \Omega_p} a i_n v_{\phi_s} \, d\mathbf{x} + \int_{\Gamma_p} \frac{I_{\text{app}}}{A} v_{\phi_s} \, d\mathbf{s},$$

while simultaneously solving for  $c_s$  and satisfying (3.7).

**3.3. Temporal discretization.** For time-stepping, we use backward Euler, which is fully implicit and first-order accurate.

The accumulation terms for the liquid-phase and solid-phase concentrations are approximated by

$$(3.12) \quad \frac{\partial c_s}{\partial t} \approx \frac{c_s^{i+1} - c_s^i}{t_{i+1} - t_i},$$

$$(3.13) \quad \frac{\partial c_e}{\partial t} \approx \frac{c_e^{i+1} - c_e^i}{t_{i+1} - t_i},$$

where  $c_s^i, c_e^i$  are the approximate solutions at time  $t_i$ . The remaining terms in the spatially discretized equations are evaluated at time  $t_{i+1}$  so that the scheme is implicit.

While the spatial discretization described above is relatively simple, it is likely sufficient in most cases. In contrast, for the temporal discretization, substantial improvements in numerical accuracy and computational efficiency could be achieved through the use of higher-order and adaptive time-stepping schemes, respectively. For example, adaptive high order schemes from Sundials [31, 26] are used in PyBaMM [54], leading to very fast and stable pseudo-2D simulations. Since we are focusing on scalable solvers for pseudo-4D simulations, we only consider backward Euler for simplicity.

**3.4. Implementation details.** The discretized equations are implemented using Firedrake [29], an open-source finite element framework that enables the specification of variational formulations at a high level of abstraction. Firedrake integrates natively with PETSc [7, 5, 6], providing access to scalable nonlinear and linear solvers, including the solver strategies discussed in section 4. An additional motivation for

this choice is the availability of automated adjoint evaluation through pyadjoint [44], which is required for PDE-constrained design optimization. Firedrake has previously been used to perform topology optimization for the design of porous electrodes for electrochemical devices [48, 37, 8]. The code developed for this work is also used in ongoing studies on topology-optimizing battery electrodes.

At the time this work was conducted, Firedrake did not robustly support finite element spaces restricted to subdomains. As a result, all variables are defined over the full computational domain. In particular, the solid-phase potential and solid-phase concentration are defined everywhere, even though they are physically relevant only within electrode regions. This design choice is necessary for topology optimization, where electrode locations evolve during the optimization process [48, 37]. In contrast, many battery model implementations restrict these variables to fixed positive and negative electrode subdomains.

To avoid matrix singularities in separator or electrolyte-only regions ( $\Omega_m$ ), a small regularization value of  $1 \times 10^{-22}$  S/m is assigned to the effective solid-phase conductivity  $\sigma^{\text{eff}}$  in these regions, whereas physical conductivity values for the electrodes are on the order  $> 1$  S/m. This also effectively mimics the no-flux boundary condition at the interface between  $\Omega_m$  and the electrode domains ( $\Omega_n, \Omega_p$ ). Similarly, the particle diffusion equation is defined such that  $\partial c_s / \partial t = 0$  in regions outside the electrodes. These regularization choices were verified to have no measurable impact on the solution within the electrode regions. Recent developments in Firedrake now allow finite element spaces to be defined on subdomains [51], and future implementations may exploit this capability when topology optimization is not performed.

The solid-phase concentration diffusion equation is incorporated into the finite element framework via a variational formulation over the particle degrees of freedom; details are provided in Appendix A. Since standard continuous finite element spaces would enforce artificial continuity across the electrode domain, a piecewise constant finite element space is used for the solid-phase concentration. Specifically, each solid-phase concentration component corresponding to a discrete particle radius  $r = r_i$  is represented as a cellwise constant field on the electrode-scale mesh. While this choice leads to numerous particle-level unknowns on unstructured tetrahedral meshes, it yields a natural block structure that is well suited to the solver strategies described in section 4.

**4. Solution strategy.** In large-scale simulations involving three-dimensional PDEs, the resulting linear systems can be too large to be efficiently solved with direct solvers due to their prohibitive memory requirements and computational cost, especially at fine spatial resolutions. Due to the complexity of the P4D model, the limits of direct solvers are reached quickly. Iterative solvers offer a scalable alternative, enabling the solution of large, sparse linear systems with more favorable memory usage and better suitability for parallel computing environments. This section outlines the structure of the linear systems arising from the P4D model discretization and details the preconditioning strategies employed to achieve scalable simulations.

**4.1. Linear system structure.** After discretization, we linearize the nonlinear system (3.7) and (3.9)–(3.11) using Newton’s method. The nonlinear residual can be

written as the block residual equation

$$(4.1) \quad \mathcal{R} = \begin{bmatrix} R_{\phi_s} \\ R_{\phi_e} \\ R_{c_e} \\ R_{c_s} \end{bmatrix} = 0,$$

where  $R_{\phi_s}$  is the residual of (3.11),  $R_{\phi_e}$  is the residual of (3.10),  $R_{c_e}$  is residual of (3.9), and  $R_{c_s}$  is the residual of (3.7).

The linearization of this system results in a block matrix of this form:

$$(4.2) \quad \begin{bmatrix} A_{\phi_s, \phi_s} & A_{\phi_s, \phi_e} & A_{\phi_s, c_e} & A_{\phi_s, c_s} \\ A_{\phi_e, \phi_s} & A_{\phi_e, \phi_e} & A_{\phi_e, c_e} & A_{\phi_e, c_s} \\ A_{c_e, \phi_s} & A_{c_e, \phi_e} & A_{c_e, c_e} & A_{c_e, c_s} \\ A_{c_s, \phi_s} & A_{c_s, \phi_e} & A_{c_s, c_e} & A_{c_s, c_s} \end{bmatrix},$$

where each block  $A_{ij}$  represents the linearization of residual equation  $R_i$  with respect to variable  $j \in [\phi_s, \phi_e, c_e, c_s]$ . The blocks related to  $c_s$  are ordered point-wise according to the electrode dimension. For example, in the case of the diagonal block

$$(4.3) \quad A_{c_s, c_s} = \begin{bmatrix} (A_{c_s, c_s})_{1,1} & \cdots & (A_{c_s, c_s})_{n,n} \\ \vdots & \ddots & \vdots \\ (A_{c_s, c_s})_{n,1} & \cdots & (A_{c_s, c_s})_{n,n} \end{bmatrix} = \begin{bmatrix} (A_{c_s, c_s})_{1,1} & & & \\ & \ddots & & \\ & & \ddots & \\ & & & (A_{c_s, c_s})_{n,n} \end{bmatrix},$$

where  $(.)_{i,j}$  represents the linearization at the element  $i$  with respect to element  $j$ . Since there is no dependence between electrode-level elements for the particle equation, this is a block diagonal matrix. Each sub-block  $(A_{c_s, c_s})_{i,i}$  is an  $N_c \times N_c$  tri-diagonal matrix for the 1D finite-difference particle system at element  $i$ .

We illustrate in Figure 2 the sparsity of the full block matrix from (4.2) for a pseudo-3D (P3D) case with a  $3 \times 3$  quadrilateral mesh for the electrode-level domain and 3 points in the particle direction. We easily see the more connected structure of the finite element discretization for the top left blocks (the connectivity is even higher in 3D). The bottom right block consists of small tri-diagonal matrices, one for each element in the electrode-level mesh. The bottom left and top right sections correspond to the couplings between the electrode-level equations and the particle equation; they are sparse because they are only coupled through the solid-phase concentration at the surface.

**4.2. Preconditioning.** The linearized systems are solved iteratively using GM-RES [50]. To ensure scalability of the solution procedure, we will employ appropriate preconditioning strategies [59]. A good preconditioner is typically an approximation of the system matrix for which the inverse can be efficiently computed or approximated. For systems of coupled PDEs, considering the block structure is often key to designing a preconditioner since most available solvers will not work well when applied to the monolithic system.

A simple strategy for block systems is to consider a block diagonal preconditioner, that is, to ignore all coupling between equations:

$$(4.4) \quad P_J = \begin{bmatrix} A_{\phi_s, \phi_s} & 0 & 0 & 0 \\ 0 & A_{\phi_e, \phi_e} & 0 & 0 \\ 0 & 0 & A_{c_e, c_e} & 0 \\ 0 & 0 & 0 & A_{c_s, c_s} \end{bmatrix}.$$

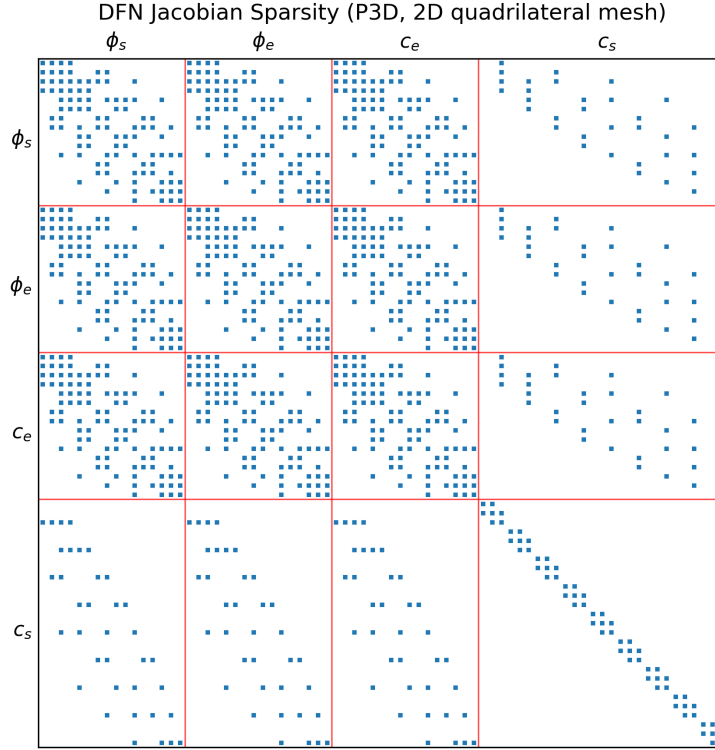


Fig. 2: Sparsity pattern of the linearized system matrix for a P3D case with a  $3 \times 3$  quadrilateral mesh for the electrode-level domain and 3 points in the particle direction.

Inverting  $P$  only requires applying the inverse of each of its blocks:

$$(4.5) \quad P_J^{-1} = \begin{bmatrix} A_{\phi_s, \phi_s}^{-1} & 0 & 0 & 0 \\ 0 & A_{\phi_e, \phi_e}^{-1} & 0 & 0 \\ 0 & 0 & A_{c_e, c_e}^{-1} & 0 \\ 0 & 0 & 0 & A_{c_s, c_s}^{-1} \end{bmatrix}.$$

This preconditioner is often referred to as block Jacobi (BJ), or in PETSc as **additive fieldsplit**.

A more expensive option is to only ignore half the couplings, leading to a block triangular preconditioner:

$$(4.6) \quad P_{GS} = \begin{bmatrix} A_{\phi_s, \phi_s} & 0 & 0 & 0 \\ A_{\phi_e, \phi_s} & A_{\phi_e, \phi_e} & 0 & 0 \\ A_{c_e, \phi_s} & A_{c_e, \phi_e} & A_{c_e, c_e} & 0 \\ A_{c_s, \phi_s} & A_{c_s, \phi_e} & A_{c_s, c_e} & A_{c_s, c_s} \end{bmatrix}.$$

While inverting  $P_{GS}$  requires more operations, it also only needs the inverse of each

diagonal block:

$$(4.7) \quad P_{GS}^{-1} = \begin{bmatrix} A_{\phi_s, \phi_s}^{-1} & 0 & 0 & 0 \\ -A_{\phi_e, \phi_e}^{-1} A_{\phi_e, \phi_s} A_{\phi_s, \phi_s}^{-1} & A_{\phi_e, \phi_e}^{-1} & 0 & 0 \\ * & * & A_{c_e, c_e}^{-1} & 0 \\ * & * & * & A_{c_s, c_s}^{-1} \end{bmatrix},$$

where the \* entries represent nested expressions involving combinations of previously inverted blocks. For example:

$$(4.8) \quad (P_{GS}^{-1})_{3,1} = -A_{c_e, c_e}^{-1} \left( A_{c_e, \phi_s} A_{\phi_s, \phi_s}^{-1} + A_{c_e, \phi_e} A_{\phi_e, \phi_e}^{-1} A_{\phi_e, \phi_s} A_{\phi_s, \phi_s}^{-1} \right),$$

and so on. This method is often referred to as block Gauss-Seidel (BGS), or in PETSc as **multiplicative fieldsplit**.

Note that for a  $4 \times 4$  block matrix, there are 24 different choices of ordering and the ordering shown above is arbitrary. In subsection 5.2, we will briefly discuss the impact of system ordering on the performance of  $P_{GS}$ .

To achieve a scalable method, the inverse of the diagonal blocks must be approximated using an iterative method instead of directly inverting them. We note that the potential blocks,  $A_{\phi_s, \phi_s}$  and  $A_{\phi_e, \phi_e}$ , are elliptic operators, and that the electrolyte concentration block  $A_{c_e, c_e}$  is a parabolic operator, meaning they are ideal candidates for a multigrid method [11]. As for the solid-phase concentration block  $A_{c_s, c_s}$ , it consists of small  $N_c \times N_c$  tri-diagonal matrices, corresponding to each mesh element. The inverse can be computed by simply inverting each small matrix, which can be done efficiently with a direct solver because these are small 1D systems. Since each small matrix corresponds to a system defined on a single element, this can be done using element-wise block Jacobi, or point block Jacobi in PETSc. Given that  $A_{c_s, c_s}$  is itself tri-diagonal, symmetric Gauss-Seidel is also a viable option as a preconditioner (results not shown here).

In section 5, we will consider the scalability of the BJ and BGS preconditioners defined in (4.4) and (4.6), respectively. In both cases the inverses of the electrode-level blocks are approximated with single Algebraic Multigrid (AMG) V-cycles [49]:

$$(4.9) \quad A_{\phi_s, \phi_s}^{-1} \approx \text{AMG}(A_{\phi_s, \phi_s}), \quad A_{\phi_e, \phi_e}^{-1} \approx \text{AMG}(A_{\phi_e, \phi_e}), \quad A_{c_e, c_e}^{-1} \approx \text{AMG}(A_{c_e, c_e}),$$

and the inverse of the particle block is computed using element-wise block Jacobi (EBJ):

$$(4.10) \quad A_{c_s, c_s}^{-1} = \text{EBJ}(A_{c_s, c_s}).$$

For AMG, we use BoomerAMG [30] from the hypre library [1]. The full PETSc solver parameters are given in Appendix B.

As noted in subsection 3.4, the solid-phase potential  $\phi_s$  and the solid-phase concentration  $c_s$  are defined and solved over the whole domain (even the separator). If these are instead defined as separate variables local to each cathode, one would get four electrode-specific blocks instead of  $A_{\phi_s, \phi_s}$  and  $A_{c_s, c_s}$ . The preconditioning strategies detailed here could easily be adapted to this formulation. The additive approach with  $P_J$  would essentially be the same since the variables defined in one electrode are not directly coupled with the ones in the other electrode. The multiplicative approach with  $P_{GS}$  would be slightly different if electrode-specific equations are solved sequentially. In the case of simulating resolved microstructures, block preconditioners with electrode-specific blocks are considered in [24].

**5. Results.** In this section, we evaluate block Jacobi (BJ) and block Gauss–Seidel (BGS) preconditioners for Pseudo-4D DFN simulations. We first describe four test cases with increasing spatial complexity. We then analyze block ordering effects for BGS. Finally, we present weak and strong scaling results for both preconditioners.

**5.1. Test cases.** We consider four different test cases with varying levels of complexity in terms of 3D spatial variations: a cubic cell with homogeneous properties (Case I), then with heterogeneous properties (Case II), a flattened jelly roll leading to a very skewed geometry (Case III), and interpenetrating gyroid electrodes with a complex geometry (Case IV).

For simplicity, all cases use the material properties from [41], corresponding to a lithium cobalt oxide cathode (positive electrode) and a graphite anode (negative electrode). All model parameters are detailed in Appendix C.

All simulations are performed for a fixed applied current density corresponding to a battery discharge at a rate of 1C. This corresponds to a theoretical full discharge in one hour, although a minimum voltage (for safety) would be reached much sooner than that. For simplicity, the simulated time is 30 minutes, which means half of a full discharge. This avoids having to take smaller time steps when approaching the minimum voltage. We fix the time-step size  $\Delta t$  to one minute, for a total of 30 steps, as a representative large step size for which the fully coupled Newton solver remains robust and converges reliably, while still resolving the macroscopic discharge dynamics of interest.

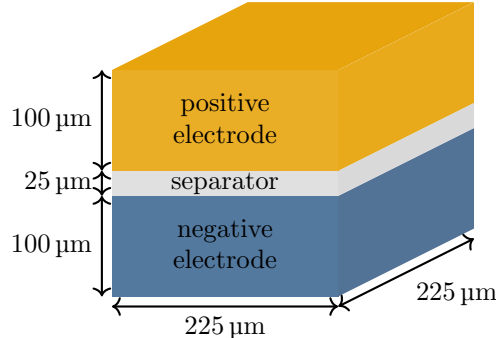


Fig. 3: Diagram of the simulation domain for Cases I and II.

**Case I: Homogeneous Cubic Cell.** Our first test case is a simple cubic cell with 100  $\mu\text{m}$  thick electrodes and a 25  $\mu\text{m}$  separator as illustrated in Figure 3. Although not representative of typical operating conditions, the applied current density is prescribed as a two-dimensional Gaussian field in order to induce three-dimensional spatial variation in what would otherwise be a 1D problem. Let  $I_{\text{app}}$  be a reference applied current, typically calculated based on the mass loading of the active material. The spatially varying applied current density  $i_{\text{app}}$  on the positive current collector  $\Gamma_p$

is given by

$$(5.1) \quad i_{\text{app}}(y, z) = \frac{I_{\text{app}}}{\int_{\Gamma_p} \exp\left(-\frac{(y - y_0)^2}{2\sigma_y^2} - \frac{(z - z_0)^2}{2\sigma_z^2}\right) dS} \exp\left(-\frac{(y - y_0)^2}{2\sigma_y^2} - \frac{(z - z_0)^2}{2\sigma_z^2}\right),$$

where  $(y_0, z_0)$  denotes the center of the collector surface, and  $\sigma_y, \sigma_z$  are the spreads in the  $y$ - and  $z$ -directions, respectively. The normalization guarantees that

$$(5.2) \quad \int_{\Gamma_p} i_{\text{app}}(y, z) ds = I_{\text{app}},$$

so that the average current density is given by  $I_{\text{app}}/A$ , where  $A = \int_{\Gamma_p} dS$  is the area of the current collector. The Gaussian profile is centered in the middle of the current collector surface,

$$(5.3) \quad y_0 = \frac{1}{2}L_y, \quad z_0 = \frac{1}{2}L_z,$$

and the standard deviations are taken as a fixed fraction of the collector dimensions,

$$(5.4) \quad \sigma_y = 0.1 L_y, \quad \sigma_z = 0.1 L_z,$$

where  $L_y = L_z = 225 \mu\text{m}$  are the lengths of the collector in the  $y$ - and  $z$ -directions, respectively.

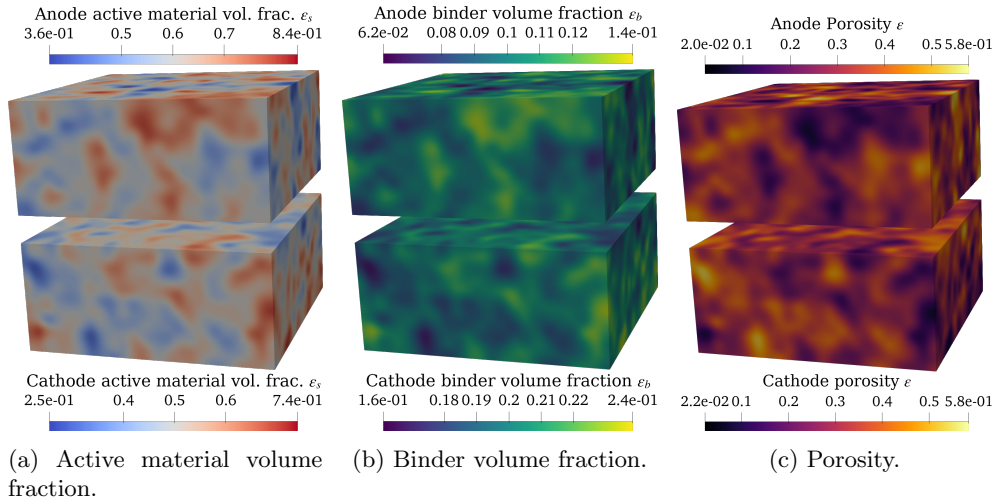


Fig. 4: Spatially varying material properties for Case II.

**Case II: Spatially Varying Properties.** Using the same geometry as Case I, we now introduce spatial variations within the domain by adding spatial heterogeneity in material properties. For the pseudo-2D DFN model, it is typical to consider constant properties since homogenization is already being performed in the other two spatial dimensions. Typically, spatially-varying properties are captured using simulations where the microstructure (active particles, binder, etc.) is resolved [66, 32, 18]

However, some electrode-scale heterogeneity (as opposed to particle-scale heterogeneity) can be captured using homogenized porous electrode theory simulations [43, 47]. In this case, the current is applied uniformly on the current collector face.

To prescribe smooth, spatially correlated heterogeneity for material volume fractions, we construct a filtered random field over the domain  $\Omega$ . A coarse, structured grid of resolution  $h_c$  is defined on  $\Omega$ , with nodes  $\{(x_i, y_j, z_k)\}_{i,j,k}$ . On this coarse grid, independent standard Gaussian samples  $g_{ijk} \sim \mathcal{N}(0, 1)$  are drawn to define a piecewise trilinear interpolant  $g(x)$  over  $\Omega$ . To introduce spatial correlation with length scale  $h_c$ , we apply a reaction-diffusion-type filter [36] to obtain a smooth field  $\tilde{g}$  by solving

$$(I - h_c^2 \nabla^2) \tilde{g} = g \quad \text{in } \Omega,$$

on the finer mesh used for the battery simulations, yielding a function  $\tilde{g}(x)$  with reduced high-frequency content. This is a Matérn type Gaussian random field [16, 23].

Table 1: Prescribed mean and variance values for volume fractions of solid components.

Component	Mean ( $\bar{\varepsilon}_i$ )	Variance ( $\sigma_i^2$ )
Active material (cathode)	0.50	0.004
Binder (cathode)	0.20	0.0001
Active material (anode)	0.60	0.004
Binder (anode)	0.10	0.0001

The field  $\tilde{g}$  is then normalized to match prescribed statistical moments. Let  $\bar{g} = \frac{1}{|\Omega|} \int_{\Omega} \tilde{g}(x) dx$  and  $\text{Var}[\tilde{g}] = \frac{1}{|\Omega|} \int_{\Omega} (\tilde{g}(x) - \bar{g})^2 dx$ . We define the rescaled field

$$\varepsilon_i(x) = \bar{\varepsilon}_i + \sqrt{\frac{\sigma_i^2}{\text{Var}[\tilde{g}]}} (\tilde{g}(x) - \bar{g}),$$

so that  $\varepsilon_i(x)$  has mean  $\bar{\varepsilon}_i$  and variance  $\sigma_i^2$ . The active-material and binder volume fractions,  $\varepsilon_s, \varepsilon_b$ , in the cathode and anode regions are generated using the  $(\bar{\varepsilon}_i, \sigma_i^2)$  values to given in Table 1. The local porosity is then computed as  $\varepsilon(x) = 1 - \varepsilon_s(x) - \varepsilon_b(x)$ .

**Case III: Flattened Jelly Roll.** A typical cylindrical lithium-ion cell employs a *jelly-roll* architecture, formed by winding stacked electrode, separator, and current collector layers around a central mandrel, as illustrated in Figure 5b. In this work, we use a flattened jelly-roll geometry obtained by unwrapping the spiral into a planar stack (Figure 5a). Since the stack thickness is negligible compared to the radius of curvature, neglecting curvature has little impact on the relevant electrochemical behavior. For simplicity, the model features single-sided electrodes rather than the more compact double-sided configuration commonly used in practical cells.

The dimensions of the simulation domain are shown in Figure 5a, not to scale. The simulation domain is quite anisotropic:  $1 \times 10^{-4} \text{ m} \times 0.05 \text{ m} \times 1 \text{ m}$ . The resulting hexahedral mesh used for strong scaling studies is also very anisotropic as mentioned in subsection 5.4.

For this case, we explicitly model the current collectors, rather than treating them as boundary surfaces as in the other cases, since the applied current is injected only through localized tabs. In these subdomains, only the solid-phase potential is solved

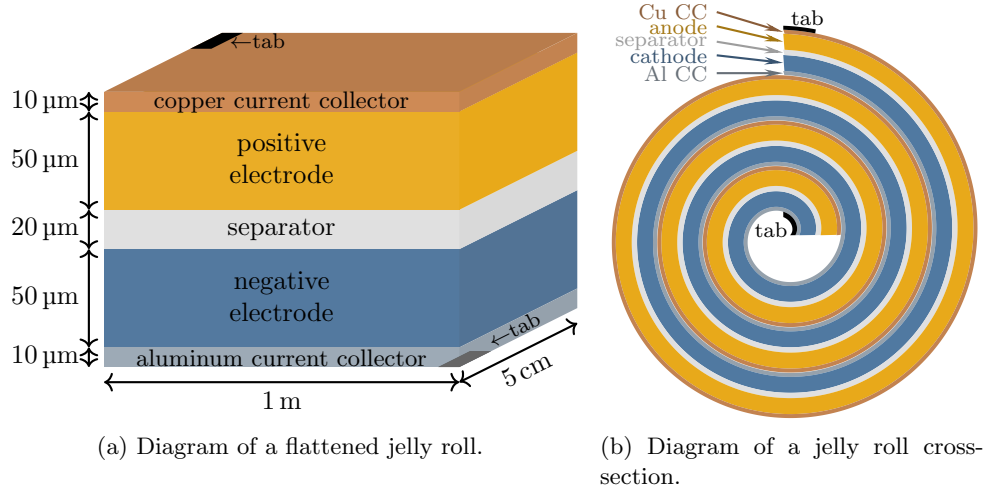


Fig. 5: Diagrams of the simulation domain of a flattened jelly roll for Case III. The diagrams are not to scale (note the dimensions in (a)). The curvature in (b) is for illustrative purposes only and is not considered in the simulations.

(2.8), with zero porosity and high solid-phase conductivity, as noted in Appendix C. The applied current and grounded potential boundary conditions (2.12) and (2.13) are imposed on tabs of dimensions  $5 \text{ mm} \times 10 \text{ mm}$  located on the current collectors. These tabs are positioned on opposite ends of the domain, corresponding to the top/bottom and interior/exterior of the rolled cell. Despite the high conductivity of the current collectors, their finite dimensions lead to nonuniform current distribution and consequently three-dimensional spatial variations.

Severe anisotropy can affect the performance of AMG. Therefore, for this case, more conservative parameters are used for BoomerAMG (e.g. less aggressive coarsening), as detail in Appendix B. In addition, we increase the GMRES restart size from the default 30 to 100.

**Case IV: Interpenetrating Gyroid.** Interpenetrating electrode architectures have recently attracted increasing attention in the energy storage literature due to their high surface-area-to-volume ratios and tunable transport pathways, leading to thick cells that are not limited by ion transport [65, 64, 61, 58].

We generate triply-periodic minimal surface (TPMS) electrode geometries in a physical computational domain  $\Omega = [0, L_x] \times [0, L_y] \times [0, L_z]$ , with  $(L_x, L_y, L_z) = (1 \text{ mm}, 1 \text{ mm}, 0.5 \text{ mm})$ , by constructing signed distance fields derived from the gyroid surface representation. Introducing dimensionless coordinates  $\hat{x} = x/L_x$ ,  $\hat{y} = y/L_y$ ,  $\hat{z} = z/L_z$ , the phase-shifted gyroid level-set functions for the two electrodes are

$$(5.5) \quad s_n(\hat{x}, \hat{y}, \hat{z}) = \sin(\pi\hat{x}) \cos(\pi\hat{y}) + \sin(\pi\hat{y}) \cos(\pi\hat{z}) + \sin(\pi\hat{z}) \cos(\pi\hat{x}) - 1.3,$$

$$(5.6) \quad s_p(\hat{x}, \hat{y}, \hat{z}) = \sin(\pi\hat{x}) \cos(\pi\hat{y} + \pi) + \sin(\pi\hat{y} + \pi) \cos(-\pi\hat{z}) + \sin(-\pi\hat{z}) \cos(\pi\hat{x}) - 1.3.$$

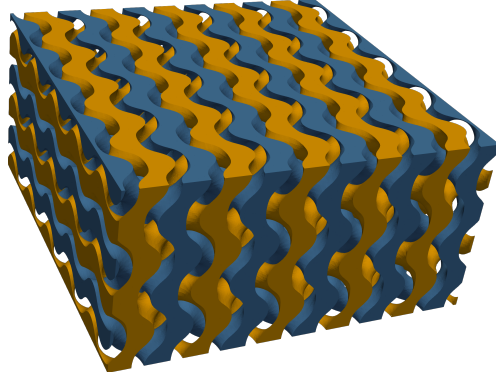


Fig. 6: Simulation domain for Case IV with TPMS gyroid electrodes where the negative electrode (anode) is orange, the positive electrode (cathode) is blue and the void in between is filled with electrolyte.

Corresponding indicator regions are defined from the signed distance inequalities

$$(5.7) \quad |s_n| \leq \frac{t}{2}, \quad |s_p| \leq \frac{t}{2},$$

with  $t = 1.104$ , yielding disjoint domains representing the anode ( $\Omega_n$ ) and cathode ( $\Omega_p$ ) phases.

To obtain a mesh conforming to the electrode-electrolyte interfaces, we solve a Target-Matrix Optimization Paradigm (TMOP) problem [21] using the MFEM framework [4]. This optimization procedure, frequently applied in level-set topology optimization, minimizes mesh distortion while aligning element faces with material interfaces [53]. This is a larger version of the electrodes and mesh used in [17].

**5.2. Impact of system ordering on block Gauss-Seidel preconditioner.** As noted in subsection 4.2, there are 24 different orderings of the  $4 \times 4$  block system and thus 24 different choices for the block Gauss-Seidel preconditioner,  $P_{GS}$  in (4.6). We tested all 24 orderings for the four cases and measured the Krylov iteration counts for the 200 processor simulations used in the strong scaling study in subsection 5.4.

Across all tests, the difference between the best and worst orderings was modest: iteration counts varied by only 6–8%, and the top five or six orderings differed by less than 2%. Two permutations,  $(\phi_e, c_s, \phi_s, c_e)$  and  $(c_e, \phi_e, c_s, \phi_s)$ , consistently ranked first or second across all geometries, indicating that the most effective orderings are robust with respect to mesh structure and local heterogeneity. All weak- and strong-scaling results reported below therefore use the  $(\phi_e, c_s, \phi_s, c_e)$  ordering. Because even the least favorable ordering increases the iteration count by only about 6–8%, the overall performance of the multiplicative block preconditioner is not highly sensitive to the ordering choice. Note that the optimal ordering could differ if material parameters or operating conditions substantially modify the relative strength of the cross-couplings, which may affect the performance of some orderings.

**5.3. Weak scaling.** We investigate the weak scalability of the BJ and BGS preconditioners by keeping the local problem size fixed at approximately  $1.4 \times 10^5$  DoFs per processor while increasing the processor count. Since mesh refinement is simpler for Case I, we use this case for the weak scaling study. Figure 7 reports the total

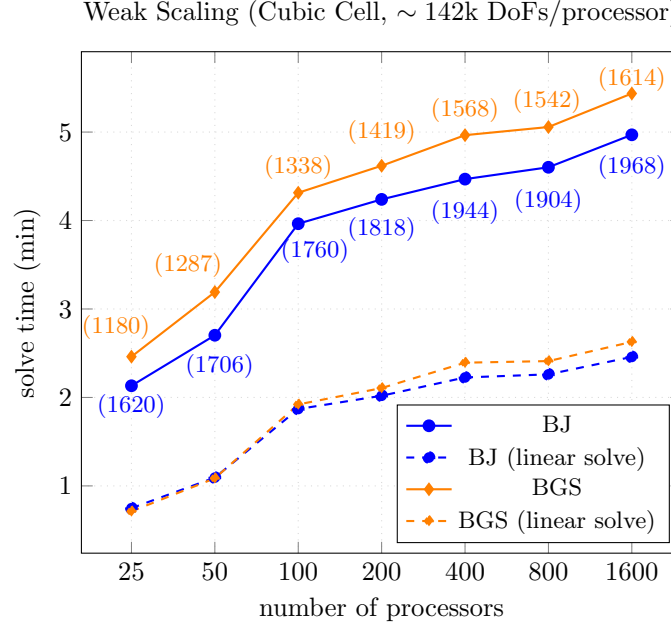


Fig. 7: Weak scaling performance with 30 time steps and approximately 142k DoFs per processor for Case I. The total number of GMRES iterations is given in parentheses.

nonlinear solve time, the time spent in the linear solve, and the corresponding GMRES iteration counts. For both BJ and BGS, the GMRES iteration counts increase only mildly between 25 and 1600 processors (approximately 36% for BJ and 21% for BGS), indicating that the preconditioners retain their effectiveness as the global problem size grows. The remaining increases in runtime are primarily due to communication overhead. The jump between 50 and 100 processors corresponds to moving from one to two sockets on the same node. The increase from 100 to 200 processors reflects the transition from intra-node to inter-node communication. Beyond this point, the total solve time grows only modestly from 200 to 1600 processors (approximately 17%), demonstrating near-ideal weak scaling for both preconditioners in this regime. The BJ preconditioner is consistently faster in total time, although BGS achieves slightly lower linear iteration counts.

**5.4. Strong scaling.** For each test case, we now perform a strong scaling study, i.e. the problem size is fixed and the number of processors is increased. The number of processors starts at 200 (2 nodes), and is doubled until 1600 processors (16 nodes). The problem size is chosen to be close to the maximum size allowed by memory requirements for the 200 processor case. Note that, at this scale, direct solvers are unfeasible due to memory requirements, so we can only test iterative solvers.

Table 2 summarizes the meshes and degrees of freedom for all test cases, including the particle-level discretization used in each case. For Cases I-III, hexahedral elements are used, with Cases I and II using identical meshes. The elements are equi-spaced in each direction. For Cases I and II, there are 207 elements in the direction of the cell thickness, so that elements are split perfectly across the positive electrode, separator, and negative domains. The other directions are 205 element-wide, leading to just

Table 2: Summary of meshes and degrees of freedom for all test cases.

Case	Mesh	Elements	Electrode DoFs	$N_c$	Particle DoFs	Total DoFs
I	Hex	$8.7 \times 10^6$	$2.6 \times 10^7$	10	$8.7 \times 10^7$	$1.13 \times 10^8$
II	Hex	$8.7 \times 10^6$	$2.6 \times 10^7$	10	$8.7 \times 10^7$	$1.13 \times 10^8$
III	Hex	$8.5 \times 10^6$	$2.6 \times 10^7$	10	$8.5 \times 10^7$	$1.12 \times 10^8$
IV	Tet	$3.6 \times 10^7$	$1.8 \times 10^7$	6	$2.18 \times 10^8$	$2.37 \times 10^8$

under 8.7 million elements, so over 26 million electrode-level degrees of freedom. In the particle-direction, we use  $N_c = 10$  points. Since in our implementation these are element-wise unknowns, we get just under 87 million particle-level degrees of freedom, for a total of over 113 million degrees of freedom. For Case III, we use 56 elements in the direction of cell thickness, 85 elements for the cell height, and 1800 elements along the length of the roll. This leads to over 8.5 million elements, so over 26 million electrode-level degrees of freedom. Again, we pick  $N_c = 10$ , leading to 85 million particle-level degrees of freedom, and thus 112 million total degrees of freedom.

For Case IV, a tetrahedral mesh with over 36 million elements is used, leading to over 18 million electrode-level degrees of freedom. For this case, we choose a smaller  $N_c = 6$  number of points in the particle direction. However, since these are element-wise unknowns, we get around 218 million particle-level degrees of freedom, for a total of 237 million degrees of freedom. Recall from subsection 4.2, that the particle system is tridiagonal, so not contributing that many non-zeros compared to the electrode-level system.

For Case I, the strong scaling results are shown in Figure 8. Both BJ and BGS exhibit substantial reductions in solve time as the processor count increases from 200 to 1600. For BJ, the total solve time decreases from approximately 1028 seconds at 200 processors to 166 seconds at 1600 processors, corresponding to a  $6.2\times$  speedup and a parallel efficiency of 0.78 relative to ideal  $8\times$  scaling. BGS shows a similar trend, decreasing from 1193 seconds to 184 seconds over the same range, yielding a  $6.5\times$  speedup and an efficiency of 0.81. The linear solve times follow the same pattern, and the GMRES iteration counts remain nearly constant (variations below 15% for BJ and 20% for BGS), indicating that the preconditioner performance is relatively robust under mesh partitioning. BJ consistently attains lower wall-clock times despite slightly higher iteration counts, while BGS incurs a higher per-iteration cost. The total solve time increases at a faster rate from 800 to 1600 processors, indicating higher communication costs. Note that at 800 processors, there are around 142k DoFs per processor, which was found to be a good balance in the weak scaling study. At 71k DoFs per processor, communication is starting to become a bottleneck.

For Case II, the strong scaling results for the heterogeneous electrodes are shown in Figure 9. Compared with the homogeneous Case I, both BJ and BGS typically require on the order of 5% more GMRES iterations, reflecting a mild increased difficulty introduced by spatial variations in the active-material and binder volume fractions. Nevertheless, both preconditioners continue to exhibit strong parallel scalability. For the BJ preconditioner, the total solve time decreases from approximately 1140 seconds at 200 processors to 220 seconds at 1600 processors, corresponding to a  $5.2\times$  speedup and a parallel efficiency of 0.65. The BGS preconditioner shows a similar reduction, decreasing from 1292 seconds to 221 seconds over the same range, yielding a  $5.9\times$  speedup and an efficiency of 0.73. The linear solve times exhibit nearly

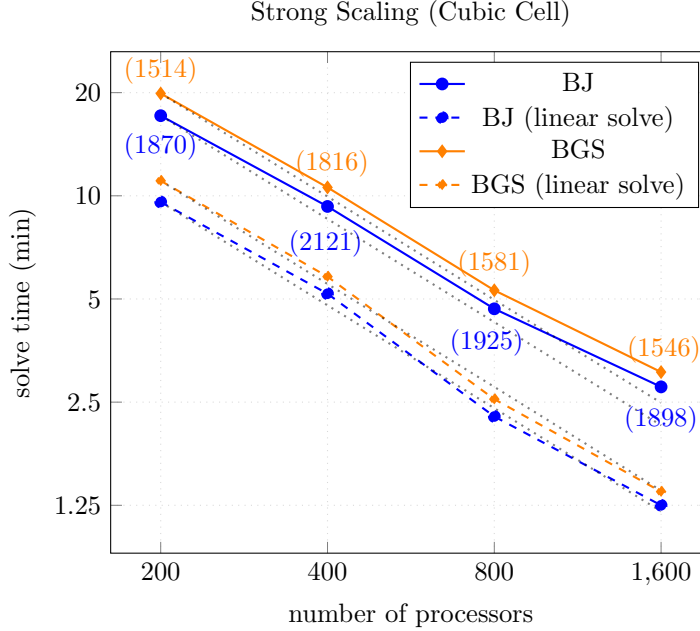


Fig. 8: Strong scaling timings for Case I, the homogeneous cubic cell problem (113M DoFs). The total number of GMRES iterations are given in parentheses. Ideal scaling is given by dotted lines.

identical trends, and iteration counts remain essentially flat across processor counts, confirming that the preconditioners remain robust despite the introduction of spatially correlated heterogeneity. As in Case I, BJ achieves the lowest wall-clock times, but BGS maintains comparable parallel efficiency and slightly lower iteration counts. Again, communication starts to become a bottleneck at 1600 processors.

For Case III, the strong scaling results for the flattened jelly-roll geometry are shown in Figure 10. The highly anisotropic domain and mesh ( $1 \times 10^{-4} \text{ m} \times 0.05 \text{ m} \times 1 \text{ m}$ ) pose additional challenges for solver performance. The BJ preconditioner reduces the total solve time from approximately 2300 seconds at 200 processors to 368 seconds at 1600 processors, corresponding to a  $6.3 \times$  speedup and a parallel efficiency of 0.79 relative to ideal  $8 \times$  scaling. The BGS preconditioner is consistently faster, decreasing from 2122 seconds to 271 seconds over the same processor range, yielding a  $7.8 \times$  speedup and an efficiency of 0.97. The anisotropy of this case degrades the performance of AMG, resulting in a substantially larger number of GMRES iterations: 30–40 per Newton iteration for BGS and 50–80 per Newton iteration for BJ. In some instances, a single Newton step requires 100–300 GMRES iterations. To assess whether this iteration growth is intrinsic to the block preconditioning strategy or driven by multigrid's poor performance, we performed additional experiments on smaller problems (not shown) in which AMG was replaced by a sparse direct (LU) solver on the block subproblems. In these tests, the number of GMRES iterations was reduced to around 10 per Newton iteration, indicating that the increased iteration counts observed here are primarily attributable to the limitations of AMG in the strongly anisotropic regime. For the large-scale simulations, however, the mem-

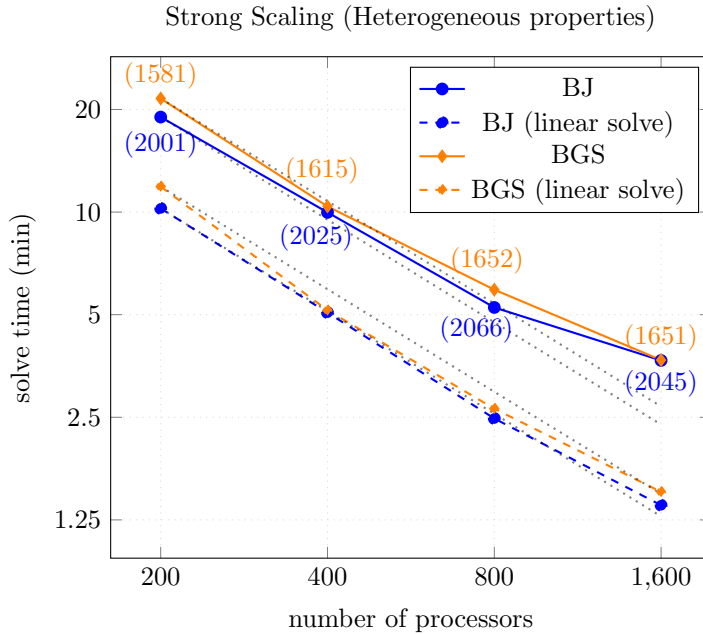


Fig. 9: Strong scaling timings for Case II, the cubic cell with heterogeneous properties (113M DoFs). The total number of GMRES iterations are given in parentheses. Ideal scaling is given by dotted lines.

ory requirements of LU factorization make this approach impractical. Overall, both preconditioners retain strong parallel scalability, with BGS exhibiting lower computational times due to reduced iteration counts. Since the total solve time in this case is dominated by the linear solver, which itself scales well, the overall strong scaling appears more favorable than in the other cases, despite the increased number of Krylov iterations. These results suggest that multigrid approaches tailored to highly anisotropic geometries could further improve solver robustness and efficiency for cases like jelly-roll cells.

Finally, for Case IV, the strong scaling results for the interpenetrating gyroid geometry are shown in Figure 11. For the BJ preconditioner, the total solve time decreases from approximately 1274 seconds at 200 processors to 272 seconds at 1600 processors, corresponding to a  $4.7\times$  speedup and a parallel efficiency of 0.59. The BGS preconditioner remains slower across all processor counts, reducing the solve time from 1833 seconds to 299 seconds over the same range, yielding a  $6.1\times$  speedup and an efficiency of 0.76. However, both preconditioners show increased sensitivity to mesh partitioning at higher core counts, particularly at 1600 processors where the iteration counts rise sharply (from 2054 to 3574 for BJ and from 1757 to 2962 for BGS). This sensitivity is consistent with the complex geometry of the TPMS and with the use of a tetrahedral mesh, which results in fewer degrees of freedom per element and therefore exposes communication bottlenecks sooner than in the hexahedral-mesh cases.

**6. Conclusion.** We have developed and evaluated scalable block preconditioning strategies for the fully implicit solution of the pseudo-4D Doyle–Fuller–Newman

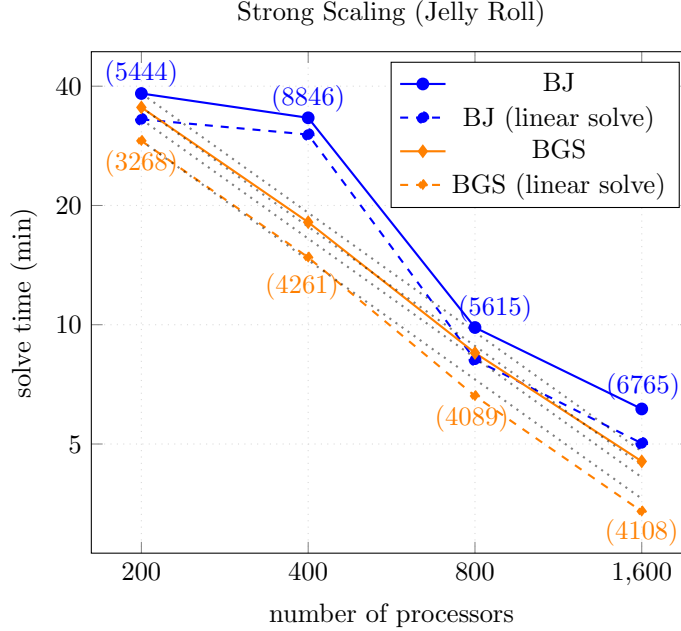


Fig. 10: Strong scaling timings for Case III, the flattened jelly roll problem (112M DoFs). The total number of GMRES iterations are given in parentheses. Ideal scaling is given by dotted lines.

(DFN) battery model in three-dimensional domains. By leveraging the block structure of the coupled electrode- and particle-scale equations, we constructed block-diagonal and block-triangular preconditioners that combine algebraic multigrid for electrode-level operators with efficient direct solvers for the particle-scale diffusion blocks.

Extensive scalability experiments were conducted on a range of battery cell geometries, including homogeneous and heterogeneous cubic cells, flattened jelly-roll architectures, and interpenetrating gyroid electrodes. In all cases, the proposed preconditioners enabled robust convergence of GMRES and strong parallel scalability, with efficient solution of systems containing up to hundreds of millions of unknowns. The block-diagonal approach usually provided lower wall-clock times, while the block-triangular variant yielded reduced iteration counts, especially for highly anisotropic domains.

These results demonstrate that fully coupled, three-dimensional pseudo-4D DFN simulations can be performed efficiently and robustly at scale using iterative solvers equipped with appropriate block preconditioners. This advances the practical applicability of high-fidelity battery modeling for realistic cell architectures and operating conditions.

#### Appendix A. Implementation details for the particle equation.

Firedrake requires equations to be solved using the finite element method. Further, there is no obvious way to implement a 4th pseudo-dimension for the particle equation. Therefore, we will consider each discrete value of the discretized solid-phase concentration as a finite element function, and manually implement a finite difference scheme using these functions.

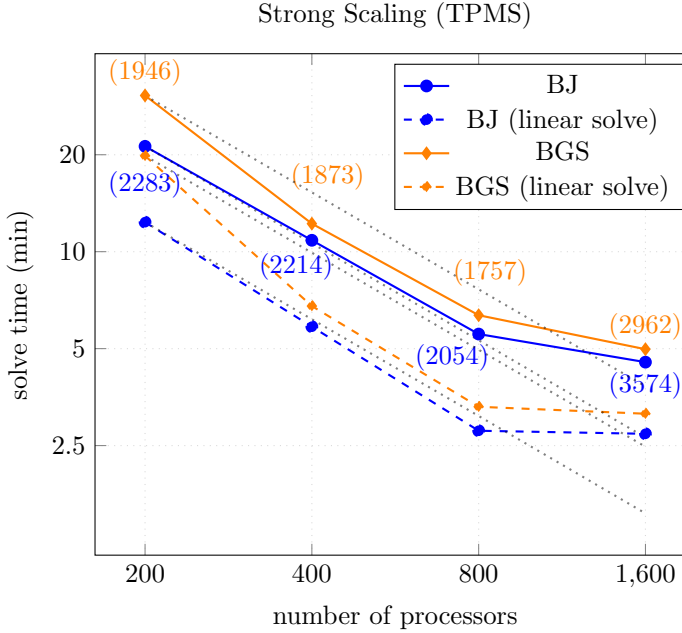


Fig. 11: Strong scaling timings for Case IV, the interdigitated gyroid electrodes problem (237M DoFs). The total number of GMRES iterations are given in parentheses. Ideal scaling is given by dotted lines.

We define a vector-valued function space  $\mathcal{V}_c = V_h^{N_c}$ , where each component corresponds to the solid-phase concentration at one radial location. The solid-phase concentration field is represented as  $\mathbf{c}_s \in \mathcal{V}_c$ , with test functions  $\mathbf{v} \in \mathcal{V}_c$  and components  $c_i, v_i$ .

We formulate the weak form by enforcing the finite difference residual at each radial node in a variational sense:

$$(A.1) \quad \int_{\Omega_n \cup \Omega_p} \left( \frac{\partial c_i}{\partial t} - \mathcal{L}_h(\mathbf{c}_s)_i \right) v_i \, d\mathbf{x} = 0, \quad \text{for } i = 1, \dots, N_c,$$

where  $\mathcal{L}_h(\mathbf{c}_s)_i$  denotes the finite difference approximation of the radial Laplacian, including boundary conditions (see (3.4)–(3.6)).

Therefore, the fully coupled variational problem is: Find  $\mathbf{c}_s \in \mathcal{V}_c$ ,  $c_e, \phi_e \in V_h$ , and  $\phi_s \in V_h^0$  such that the following (A.1) and (3.9)–(3.11) are satisfied for all test functions  $\mathbf{v} \in \mathcal{V}_c$ ,  $v_{c_e}, v_{\phi_e} \in V_h$ , and  $v_{\phi_s} \in V_h^0$ .

The weak form (A.1) is implemented directly in Firedrake by defining  $\mathbf{c}_s$  using a `VectorFunctionSpace`, evaluating the finite difference operators symbolically over the components, and associating one test function per radial node. Because the number of radial points  $N_c$  is small (typically 5–20), this approach remains computationally efficient and maintains a unified finite element representation of the full battery system.

## Appendix B. Solver parameters.

Here we provide the PETSc options used to construct the solvers for described in section 4. Note that we are using the default parameters for the nonlinear solver.

Listing 1: PETSc solver options.

```

1 % Outer Krylov solver
2 "ksp_type": "gmres",
3 "ksp_gmres_restart": 30, # or 100 for Case III
4
5 % Block preconditioner
6 "pc_type": "fieldsplit",
7 "pc_fieldsplit_type": "multiplicative", % or "additive"
8 "mat_type": "aij",
9
10 % Ordering used for the results in this paper
11 "fieldsplit_0_fields": i_phie, # index for phi_e
12 "fieldsplit_1_fields": i_cs, # index for c_s
13 "fieldsplit_2_fields": i_phis, # index for phi_s
14 "fieldsplit_3_fields": i_ce, # index for c_e
15
16 % AMG parameters. Repeat for each electrode-level block
17 % For Cases I, II, IV
18 "fieldsplit_[i)": { % replace i by i_ce, i_phie, and i_phis
19     "pc_type": "hypre",
20     "pc_hypre_boomeramg": {
21         "strong_threshold": 0.7,
22         "coarsen_type": "HMIS",
23         "agg_nl": 3,
24         "interp_type": "ext+i",
25         "agg_num_paths": 5,
26     },
27 },
28 % For Case, III
29 "fieldsplit_[i)": {
30     "pc_type": "hypre",
31     "pc_hypre_boomeramg": {
32         "strong_threshold": 0.9,
33         "coarsen_type": "HMIS",
34         "agg_nl": 0,
35         "interp_type": "ext+i",
36     },
37 }
38
39
40 % Preconditioner for particle system
41 "fieldsplit_[i_cs)": {
42     "pc_type": "pbjacobi",
43 },

```

### Appendix C. Model Parameters.

This appendix summarizes all parameters used in the Doyle–Fuller–Newman (DFN) model described in section 2. All parameter values are from [41], taken directly from PyBaMM [54].

Table 3: Universal physical constants.

Symbol	Description	Value	Unit
$F$	Faraday constant	96485.33	$\text{C mol}^{-1}$
$R$	Ideal gas constant	8.31446	$\text{J mol}^{-1} \text{K}^{-1}$
$T$	Temperature	298.15	K

Table 4: Electrolyte parameters.

Symbol	Description	Value	Unit
$c_{e,0}$	Initial electrolyte concentration	1000	$\text{mol m}^{-3}$
$t_+^0$	Cation transference number	0.4	-
$b$	Bruggeman exponent	1.5	-
$D_e(c_e, T)$	Bulk electrolyte diffusivity	see (C.1)	-
$\kappa(c_e, T)$	Bulk electrolyte conductivity	see (C.2)	-

(C.1)

$$D_e(c_e, T) = 5.34 \times 10^{-10} \exp\left(-0.65 \frac{c_e}{1000}\right) \exp\left(\frac{E_{D_e}}{R} \left(\frac{1}{298.15} - \frac{1}{T}\right)\right),$$

(C.2)

$$\kappa(c_e, T) = \exp\left(\frac{34700}{R} \left(\frac{1}{298.15} - \frac{1}{T}\right)\right) (0.0911 + 1.9101c - 1.052c^2 + 0.1554c^3),$$

where  $c = c_e/1000$  is the electrolyte concentration in  $\text{mol L}^{-1}$  and  $E_{D_e} = 37040 \text{ J mol}^{-1}$ .

Table 5: Cathode (positive electrode) parameters.

Symbol	Description	Value	Unit
$\varepsilon_s$	Active material volume fraction	0.5	-
$\varepsilon$	Porosity	0.3	-
$\sigma$	Solid-phase conductivity	10	$\text{S m}^{-1}$
$k$	Reaction rate constant	$6 \times 10^{-7}$	$\text{A/m}^2 (\text{m}^3/\text{mol})^{1.5}$
$\alpha_a = \alpha_c$	Charge-transfer coefficients	0.5	-
$c_{s,\max}$	Maximum solid-phase concentration	$5.12 \times 10^4$	$\text{mol m}^{-3}$
$c_{s,0}$	Initial solid-phase concentration	$3.07 \times 10^4$	$\text{mol m}^{-3}$
$a$	Specific interfacial area	$1.5 \times 10^5$	$\text{m}^2 \text{m}^{-3}$
$D_s$	Solid diffusivity	$1.0 \times 10^{-13}$	$\text{m}^2 \text{s}^{-1}$
$R_s$	Particle radius	$1.0 \times 10^{-5}$	m
$U_{\text{ocp}}$	Open-circuit potential	see (C.3)	-

Effective transport coefficients are obtained via Bruggeman corrections as described in section 2.

The interfacial kinetics use  $U_{\text{ocp}}(c_s^{\text{surf}})$  evaluated as a function of the particle surface concentration. Let the (surface) stoichiometry

$$\theta = \frac{c_s^{\text{surf}}}{c_{s,\max}}.$$

Table 6: Anode (negative electrode) parameters.

Symbol	Description	Value	Unit
$\varepsilon_s$	Active material volume fraction	0.6	-
$\varepsilon$	Porosity	0.3	-
$\sigma$	Solid-phase conductivity	100	$\text{S m}^{-1}$
$k$	Reaction rate constant	$2 \times 10^{-5}$	$\text{A/m}^2 (\text{m}^3/\text{mol})^{1.5}$
$\alpha_a = \alpha_c$	Charge-transfer coefficients	0.5	-
$c_{s,\max}$	Maximum solid-phase concentration	$2.50 \times 10^4$	$\text{mol m}^{-3}$
$c_{s,0}$	Initial solid-phase concentration	$2.00 \times 10^4$	$\text{mol m}^{-3}$
$a$	Specific interfacial area	$1.8 \times 10^5$	$\text{m}^2 \text{m}^{-3}$
$D_s$	Solid diffusivity	$3.9 \times 10^{-14}$	$\text{m}^2 \text{s}^{-1}$
$R_s$	Particle radius	$1.0 \times 10^{-5}$	m
$U_{\text{ocp}}$	Open-circuit potential	see (C.4)	-

Table 7: Separator parameters.

Symbol	Description	Value	Unit
$\varepsilon$	Porosity	1.0	-
$\sigma$	Solid-phase conductivity	$0^\dagger$	$\text{S m}^{-1}$

$^\dagger$  This is the physical value; a small non-zero value is chosen for the effective solid-phase conductivity  $\sigma^{\text{eff}}$  for numerical reasons. See subsection 3.4 for details.

The cathode ( $\text{LiCoO}_2$ ) open-circuit potential is

$$\begin{aligned}
 U_{\text{ocp}}(\theta) = & 2.16216 + 0.07645 \tanh(30.834 - 54.4806 \tilde{\theta}) \\
 & + 2.1581 \tanh(52.294 - 50.294 \tilde{\theta}) \\
 & - 0.14169 \tanh(11.0923 - 19.8543 \tilde{\theta}) + 0.2051 \tanh(1.4684 - 5.4888 \tilde{\theta}) \\
 (C.3) \quad & + 0.2531 \tanh\left(\frac{-\tilde{\theta} + 0.56478}{0.1316}\right) - 0.02167 \tanh\left(\frac{\tilde{\theta} - 0.525}{0.006}\right),
 \end{aligned}$$

where  $\tilde{\theta} = 1.062 \theta$ .

The anode (graphite) open-circuit potential is

$$\begin{aligned}
 U_{\text{ocp}}(\theta) = & 0.194 + 1.5 \exp(-120\theta) + 0.0351 \tanh\left(\frac{\theta - 0.286}{0.083}\right) \\
 & - 0.0045 \tanh\left(\frac{\theta - 0.849}{0.119}\right) - 0.035 \tanh\left(\frac{\theta - 0.9233}{0.05}\right) \\
 & - 0.0147 \tanh\left(\frac{\theta - 0.5}{0.034}\right) - 0.102 \tanh\left(\frac{\theta - 0.194}{0.142}\right) \\
 & - 0.022 \tanh\left(\frac{\theta - 0.9}{0.0164}\right) - 0.011 \tanh\left(\frac{\theta - 0.124}{0.0226}\right) \\
 (C.4) \quad & + 0.0155 \tanh\left(\frac{\theta - 0.105}{0.029}\right).
 \end{aligned}$$

Table 8: Current collector parameters for Case III.

Material	Description	Value	Unit
Aluminum	Electrical conductivity	$3.77 \times 10^7$	$\text{S m}^{-1}$
Copper	Electrical conductivity	$5.96 \times 10^7$	$\text{S m}^{-1}$

To define the applied current corresponding to a 1C discharge, we compute the *theoretical* (i.e., maximum) cell capacity from the active-material lithium inventory in each porous electrode. Let  $V_n$  and  $V_p$  be the volume of the negative and positive electrode domains, respectively. Given the solid volume fraction  $\varepsilon_{s,i}$  and the maximum lithium concentration in the solid phase  $c_{s,i}^{\max}$  (in  $\text{mol m}^{-3}$  of solid), the theoretical capacity of electrode  $i$  (in ampere-hours) is computed as

$$(C.5) \quad Q_i = \frac{F}{3600} \varepsilon_{s,i} V_i c_{s,i}^{\max}, \quad i \in \{n, p\},$$

where constant and the factor 3600 converts coulombs to ampere-hours. The theoretical cell capacity is taken as the minimum of the electrode capacities,

$$(C.6) \quad Q = \min\{Q_n, Q_p\},$$

so that the limiting electrode determines the maximum cyclable lithium inventory.

Finally, for a prescribed C-rate  $C$ , we define the applied current magnitude as

$$(C.7) \quad I_{\text{app}} = C Q,$$

where  $C = 1$  is chosen for all simulations.

Note that in our configuration, the electrodes are assigned equal geometric volumes and solid volume fractions, which results in  $Q_n < Q_p$  due to the smaller maximum lithium concentration of the graphite anode. In contrast, commercial lithium-ion cells typically employ an oversized anode, so that the cathode is capacity-limiting and  $Q_p < Q_n$ .

- [1] *hypre: High performance preconditioners.* <https://computation.llnl.gov/projects/hypre-scalable-linear-solvers-multigrid-methods>.
- [2] C. AIKEN, N. KOWALSKI, R. C. FITZNER, S. TRUSSLER, J. HARLOW, E. J. BUTLER, AND J. DAHN, *Tracking electrolyte motion in cylindrical Li-ion cells using moment of inertia measurements*, Journal of the Electrochemical Society, 170 (2023), p. 040529, <https://doi.org/10.1149/1945-7111/acce72>.
- [3] J. M. ALLEN, J. CHANG, F. L. USSEGLIO-VIRETTA, P. GRAF, AND K. SMITH, *A segregated approach for modeling the electrochemistry in the 3-D microstructure of Li-ion batteries and its acceleration using block preconditioners*, Journal of Scientific Computing, 86 (2021), p. 42, <https://doi.org/10.1007/s10915-021-01410-5>.
- [4] R. ANDERSON, J. ANDREJ, A. BARKER, J. BRAMWELL, J. S. CAMIER, J. CERVENY, V. DOBREV, Y. DUDOUIT, A. FISHER, T. KOLEV, W. PAZNER, M. STOWELL, V. TOMOV, I. AKKERMAN, J. DAHM, D. MEDINA, AND S. ZAMPINI, *MFEM: A modular finite element methods library*, Computers and Mathematics with Applications, 81 (2021), pp. 42–74, <https://doi.org/10.1016/j.camwa.2020.06.009>.
- [5] S. BALAY, S. ABHYANKAR, M. F. ADAMS, S. BENSON, J. BROWN, P. BRUNE, K. BUSCHELMAN, E. CONSTANTINESCU, L. DALCIN, A. DENER, V. EIJKHOUT, J. FAIBUSSOWITSCH, W. D. GROPP, V. HAPLA, T. ISAAC, P. JOLIVET, D. KARPEEV, D. KAUSHIK, M. G. KNEPLEY, F. KONG, S. KRUGER, D. A. MAY, L. C. MCINNES, R. T. MILLS, L. MITCHELL, T. MUNSON, J. E. ROMAN, K. RUPP, P. SANAN, J. SARICH, B. F. SMITH, H. SUH, S. ZAMPINI, H. ZHANG, H. ZHANG, AND J. ZHANG, *PETSc/TAO users manual*, Tech. Report ANL-21/39 - Revision 3.24, Argonne National Laboratory, 2025, <https://doi.org/10.2172/2998643>.
- [6] S. BALAY, S. ABHYANKAR, M. F. ADAMS, S. BENSON, J. BROWN, P. BRUNE, K. BUSCHELMAN, E. M. CONSTANTINESCU, L. DALCIN, A. DENER, V. EIJKHOUT, J. FAIBUSSOWITSCH, W. D. GROPP, V. HAPLA, T. ISAAC, P. JOLIVET, D. KARPEEV, D. KAUSHIK, M. G. KNEPLEY, F. KONG, S. KRUGER, D. A. MAY, L. C. MCINNES, R. T. MILLS, L. MITCHELL, T. MUNSON, J. E. ROMAN, K. RUPP, P. SANAN, J. SARICH, B. F. SMITH, S. ZAMPINI, H. ZHANG, H. ZHANG, AND J. ZHANG, *PETSc Web page*. <https://petsc.org/>, 2025, <https://petsc.org/>.
- [7] S. BALAY, W. D. GROPP, L. C. MCINNES, AND B. F. SMITH, *Efficient management of parallelism in object oriented numerical software libraries*, in Modern Software Tools in Scientific Computing, E. Arge, A. M. Bruaset, and H. P. Langtangen, eds., Birkhäuser Press, 1997, pp. 163–202.
- [8] M. BARZEGARI AND A. FORNER-CUENCA, *Topology optimization of porous electrodes for electrochemical flow reactors using the finite element method and triply periodic minimal surfaces*, Chemical Engineering Journal, 512 (2025), p. 161815, <https://doi.org/10.1016/j.cej.2025.161815>.
- [9] M. D. R. BATISTA, S. CHANDRASEKARAN, B. D. MORAN, M. S. DE TROYA, A. PINONGCOS, Z. WANG, R. HENSLEIGH, A. CARLETON, M. ZENG, T. ROY, ET AL., *Design and additive manufacturing of optimized electrodes for energy storage applications*, Carbon, 205 (2023), pp. 262–269, <https://doi.org/10.1016/j.carbon.2023.01.044>.
- [10] T. BOND, S. GASILOV, R. DRESSLER, R. PETIBON, S. HY, AND J. DAHN, *Operando 3D imaging of electrolyte motion in cylindrical Li-ion cells*, Journal of The Electrochemical Society, 172 (2025), p. 030512, <https://doi.org/10.1149/1945-7111/adbaf>.
- [11] A. BRANDT, *Multi-level adaptive solutions to boundary-value problems*, Mathematics of Computation, 31 (1977), pp. 333–390, <https://doi.org/10.1090/s0025-5718-1977-0431719-x>.
- [12] F. BROS A PLANELLA, W. AI, A. M. BOYCE, A. GHOSH, I. KOROTKIN, S. SAHU, V. SULZER, R. TIMMS, T. G. TRANTER, M. ZYSKIN, ET AL., *A continuum of physics-based lithium-ion battery models reviewed*, Progress in Energy, 4 (2022), p. 042003, <https://doi.org/10.1088/2516-1083/ac7d31>.
- [13] V. D. BRUGGEMAN, *Berechnung verschiedener physikalischer konstanten von heterogenen substanzen. i. dielektrizitätskonstanten und leitfähigkeiten der mischkörper aus isotropen substanzen*, Annalen der physik, 416 (1935), pp. 636–664, <https://doi.org/10.1002/andp.19354160705>.
- [14] G. BUCCI, Y.-M. CHIANG, AND W. C. CARTER, *Formulation of the coupled electrochemical-mechanical boundary-value problem, with applications to transport of multiple charged species*, Acta Materialia, 104 (2016), pp. 33–51, <https://doi.org/10.1016/j.actamat.2015.11.030>.
- [15] COMSOL AB, *COMSOL Multiphysics® v. 6.2*, Stockholm, Sweden, 2023, <https://www.comsol.com>.
- [16] M. CROCI, M. B. GILES, M. E. ROGNES, AND P. E. FARRELL, *Efficient white noise sampling and coupling for multilevel Monte Carlo with nonnested meshes*, SIAM/ASA Journal on Uncertainty Quantification, 6 (2018), pp. 1630–1655, <https://doi.org/10.1137/18M1175239>.

- [17] N. R. CROSS, H. LI, T. ROY, V. M. EHLINGER, T. Y. LIN, N. W. BRADY, S. CHANDRASEKARAN, M. A. WORSLEY, AND G. BUCCI, *Viability of additively manufactured electrodes for lithium-ion batteries*, ACS Applied Engineering Materials, 3 (2024), pp. 214–224, <https://doi.org/10.1021/acsaenm.4c00717>.
- [18] T. DANNER, M. SINGH, S. HEIN, J. KAISER, H. HAHN, AND A. LATZ, *Thick electrodes for lithium batteries: A model based analysis*, Journal of Power Sources, 334 (2016), pp. 191–201, <https://doi.org/10.1016/j.jpowsour.2016.09.143>.
- [19] DASSAULT SYSTÈMES SIMULIA CORP., *Abaqus Analysis User's Guide, version 2024*, Providence, RI, USA, 2024.
- [20] P. DI PRIMA, D. DESSANTIS, D. VERSACI, J. AMICI, S. BODOARDO, AND M. SANTARELLI, *Understanding calendar aging degradation in cylindrical lithium-ion cell: A novel pseudo-4-dimensional electrochemical-thermal model*, Applied Energy, 377 (2025), p. 124640, <https://doi.org/10.1016/j.apenergy.2024.124640>.
- [21] V. DOBREV, P. KNUPP, T. KOLEV, K. MITTAL, AND V. TOMOV, *The target-matrix optimization paradigm for high-order meshes*, SIAM Journal on Scientific Computing, 41 (2019), pp. B50–B68, <https://doi.org/10.1137/18M1167206>.
- [22] M. DOYLE, T. F. FULLER, AND J. NEWMAN, *Modeling of galvanostatic charge and discharge of the lithium/polymer/insertion cell*, Journal of The Electrochemical Society, 140 (1993), pp. 1526–1533, <https://doi.org/10.1149/1.2221597>.
- [23] T. DUSWALD, B. KEITH, B. LAZAROV, S. PETRIDES, AND B. WOHLMUTH, *Finite elements for Matérn-type random fields: Uncertainty in computational mechanics and design optimization*, Computer Methods in Applied Mechanics and Engineering, 429 (2024), p. 117146, <https://doi.org/10.1016/j.cma.2024.117146>.
- [24] R. FANG, M. KRONBICHLER, M. WURZER, AND W. A. WALL, *Parallel, physics-oriented, monolithic solvers for three-dimensional, coupled finite element models of lithium-ion cells*, Computer Methods in Applied Mechanics and Engineering, 350 (2019), pp. 803–835, <https://doi.org/10.1016/j.cma.2019.03.017>.
- [25] T. F. FULLER, M. DOYLE, AND J. NEWMAN, *Simulation and optimization of the dual lithium ion insertion cell*, Journal of the electrochemical society, 141 (1994), p. 1, <https://doi.org/10.1149/1.2054684>.
- [26] D. J. GARDNER, D. R. REYNOLDS, C. S. WOODWARD, AND C. J. BALOS, *Enabling new flexibility in the SUNDIALS suite of nonlinear and differential/algebraic equation solvers*, ACM Transactions on Mathematical Software (TOMS), (2022), <https://doi.org/10.1145/3539801>.
- [27] H. GUNNARSSON, *Architectured materials for structural battery: Tailored porosity with triply periodic minimal surfaces*, master's thesis, Chalmers University of Technology, Gothenburg, Sweden, 2023.
- [28] Y. HAHN, Z. GAO, T.-T. NGUYEN, AND V. OANCEA, *A reduced order model for a lithium-ion 3D pouch battery for coupled thermal-electrochemical analysis*, Journal of Energy Storage, 70 (2023), p. 107966, <https://doi.org/10.1016/j.est.2023.107966>.
- [29] D. A. HAM, P. H. J. KELLY, L. MITCHELL, C. J. COTTER, R. C. KIRBY, K. SAGIYAMA, N. BOUZIANI, S. VORDERWUELBECKE, T. J. GREGORY, J. BETTERIDGE, D. R. SHAPERO, R. W. NIXON-HILL, C. J. WARD, P. E. FARRELL, P. D. BRUBECK, I. MARSDEN, T. H. GIBSON, M. HOMOLYA, T. SUN, A. T. T. MCRAE, F. LUPORINI, A. GREGORY, M. LANGE, S. W. FUNKE, F. RATHGEBER, G.-T. BERCEA, AND G. R. MARKALL, *Firedrake User Manual*, Imperial College London and University of Oxford and Baylor University and University of Washington, first edition ed., 5 2023, <https://doi.org/10.25561/104839>.
- [30] V. E. HENSON AND U. M. YANG, *BoomerAMG: A parallel algebraic multigrid solver and preconditioner*, Appl. Numer. Math., 41 (2002), p. 155–177, [https://doi.org/10.1016/S0168-9274\(01\)00115-5](https://doi.org/10.1016/S0168-9274(01)00115-5).
- [31] A. C. HINDMARSH, P. N. BROWN, K. E. GRANT, S. L. LEE, R. SERBAN, D. E. SHUMAKER, AND C. S. WOODWARD, *SUNDIALS: Suite of nonlinear and differential/algebraic equation solvers*, ACM Transactions on Mathematical Software (TOMS), 31 (2005), pp. 363–396, <https://doi.org/10.1145/1089014.1089020>.
- [32] T. HUTZENLAUB, S. THIELE, N. PAUST, R. SPOTNITZ, R. ZENGERLE, AND C. WALCHSHOFER, *Three-dimensional electrochemical Li-ion battery modelling featuring a focused ion-beam/scanning electron microscopy based three-phase reconstruction of a LiCoO<sub>2</sub> cathode*, Electrochimica Acta, 115 (2014), pp. 131–139, <https://doi.org/10.1016/j.electacta.2013.10.103>.
- [33] S. JUNG AND D. KANG, *Multi-dimensional modeling of large-scale lithium-ion batteries*, Journal of Power Sources, 248 (2014), pp. 498–509, <https://doi.org/10.1016/j.jpowsour.2013.09.103>.

- [34] R. KANTHARAJ AND A. M. MARCONNET, *Heat generation and thermal transport in lithium-ion batteries: a scale-bridging perspective*, Nanoscale and Microscale Thermophysical Engineering, 23 (2019), pp. 128–156, <https://doi.org/10.1080/15567265.2019.1572679>.
- [35] S. KULATHU, J. A. HURTADO, K. BOSE, Y. HAHN, P. A. BOUZINOV, R. L. TAYLOR, AND V. OANCEA, *A three-dimensional thermal-electrochemical-mechanical-porous flow multi-scale formulation for battery cells*, International Journal for Numerical Methods in Engineering, 125 (2024), p. e7464, <https://doi.org/10.1002/nme.7464>.
- [36] B. S. LAZAROV AND O. SIGMUND, *Filters in topology optimization based on Helmholtz-type differential equations*, International Journal for Numerical Methods in Engineering, 86 (2011), pp. 765–781, <https://doi.org/10.1002/nme.3072>.
- [37] H. LI, G. BUCCI, N. W. BRADY, N. R. CROSS, V. M. EHLINGER, T. Y. LIN, M. SALAZAR DE TROYA, D. TORTORELLI, M. A. WORSLEY, AND T. ROY, *Topology optimization for the full-cell design of porous electrodes in electrochemical energy storage devices*, Structural and Multidisciplinary Optimization, 67 (2024), p. 188, <https://doi.org/10.1007/s00158-024-03901-z>.
- [38] J. LIN, H. N. CHU, K. THU, M. WOJTALA, F. GAO, AND K. J. CHUA, *Novel battery thermal management via scalable dew-point evaporative cooling*, Energy Conversion and Management, 283 (2023), p. 116948, <https://doi.org/10.1016/j.enconman.2023.116948>.
- [39] T. Y. LIN, H. LI, N. W. BRADY, N. R. CROSS, V. M. EHLINGER, T. ROY, D. TORTORELLI, C. ORME, M. A. WORSLEY, AND G. BUCCI, *Shape matters: understanding the effect of electrode geometry on cell resistance and chemo-mechanical stress*, Journal of the Electrochemical Society, 171 (2024), p. 100515, <https://doi.org/10.1149/1945-7111/ad81b4>.
- [40] B. LIU, H. ZHAO, H. YU, J. LI, AND J. XU, *Multiphysics computational framework for cylindrical lithium-ion batteries under mechanical abusive loading*, Electrochimica Acta, 256 (2017), pp. 172–184, <https://doi.org/10.1016/j.electacta.2017.10.045>.
- [41] S. G. MARQUIS, V. SULZER, R. TIMMS, C. P. PLEASE, AND S. J. CHAPMAN, *An asymptotic derivation of a single particle model with electrolyte*, Journal of The Electrochemical Society, 166 (2019), p. A3693, <https://doi.org/10.1149/2.0341915jes>.
- [42] W. MEI, C. LIANG, J. SUN, AND Q. WANG, *Three-dimensional layered electrochemical-thermal model for a lithium-ion pouch cell*, International Journal of Energy Research, 44 (2020), pp. 8919–8935, <https://doi.org/10.1002/er.5601>.
- [43] A. MISTRY, K. SMITH, AND P. P. MUKHERJEE, *Stochasticity at scales leads to lithium intercalation cascade*, ACS Applied Materials & Interfaces, 12 (2020), pp. 16359–16366, <https://doi.org/10.1021/acsami.9b23155>.
- [44] S. K. MITUSCH, S. W. FUNKE, AND J. S. DOKKEN, *dolfin-adjoint 2018.1: automated adjoints for FEniCS and Firedrake*, Journal of Open Source Software, 4 (2019), p. 1292, <https://doi.org/10.21105/joss.01292>.
- [45] J. NEWMAN, *Numerical solution of coupled, ordinary differential equations*, Industrial & Engineering Chemistry Fundamentals, 7 (1968), pp. 514–517, <https://doi.org/10.1021/i160027a025>.
- [46] J. NEWMAN, *Dualfoil*. <http://www.cchem.berkeley.edu/jsngrp/fortran.html>, 1998.
- [47] M. PARMANANDA, C. NORRIS, S. A. ROBERTS, AND P. P. MUKHERJEE, *Probing the role of multi-scale heterogeneity in graphite electrodes for extreme fast charging*, ACS Applied Materials & Interfaces, 14 (2022), pp. 18335–18352.
- [48] T. ROY, M. A. SALAZAR DE TROYA, M. A. WORSLEY, AND V. A. BECK, *Topology optimization for the design of porous electrodes*, Structural and Multidisciplinary Optimization, 65 (2022), p. 171, <https://doi.org/10.1007/s00158-022-03249-2>.
- [49] J. W. RUGE AND K. STÜBEN, *Algebraic multigrid*, in Multigrid methods, vol. 3 of Frontiers in Applied Mathematics, SIAM, Philadelphia, 1987, ch. 4, pp. 73–130, <https://doi.org/10.1137/1.9781611971057.ch4>.
- [50] Y. SAAD AND M. H. SCHULTZ, *GMRES: A generalized minimal residual algorithm for solving nonsymmetric linear systems*, SIAM Journal on scientific and statistical computing, 7 (1986), pp. 856–869, <https://doi.org/10.1137/0907058>.
- [51] K. SAGIYAMA, L. MITCHELL, AND D. A. HAM, *An abstraction for solving multi-domain problems using finite element methods*, arXiv preprint arXiv:2512.06146, (2025), <https://doi.org/10.48550/arXiv.2512.06146>.
- [52] A. SAMBA, N. OMAR, H. GUALOUS, O. CAPRON, P. VAN DEN BOSSCHE, AND J. VAN MIERLO, *Impact of tab location on large format lithium-ion pouch cell based on fully coupled three-dimensional electrochemical-thermal modeling*, Electrochimica Acta, 147 (2014), pp. 319–329, <https://doi.org/10.1016/j.electacta.2014.08.115>.
- [53] M. R. SCHMIDT, J. L. BARRERA, K. MITTAL, K. E. SWARTZ, AND D. A. TORTORELLI, *Level-set topology optimization with PDE generated conformal meshes*, Structural and Multidisciplinary Optimization, 65 (2022), p. 171, <https://doi.org/10.1007/s00158-022-03249-2>.

plinary Optimization, 67 (2024), p. 184, <https://doi.org/10.1007/s00158-024-03870-3>.

[54] V. SULZER, S. G. MARQUIS, R. TIMMS, M. ROBINSON, AND S. J. CHAPMAN, *Python Battery Mathematical Modelling (PyBaMM)*, Journal of Open Research Software, 9 (2021), p. 14, <https://doi.org/10.5334/jors.309>.

[55] H. SUNDQVIST AND G. VERONIS, *A simple finite-difference grid with non-constant intervals*, Tellus, 22 (1970), pp. 26–31, <https://doi.org/10.3402/tellusa.v22i1.10155>.

[56] J. THIBAULT, S. BERGERON, AND H. W. BONIN, *On finite-difference solutions of the heat equation in spherical coordinates*, Numerical Heat Transfer, 12 (1987), pp. 457–474, <https://doi.org/10.1080/1040778708913597>.

[57] T. WALDMANN, R.-G. SCURTU, D. BRÄNDLE, AND M. WOHLFAHRT-MEHRENS, *Effects of tab design in 21700 Li-ion cells: improvements of cell impedance, rate capability, and cycling aging*, Energy Technology, 11 (2023), p. 2200583, <https://doi.org/10.1002/ente.202200583>.

[58] Z. WANG, H. LI, D. HAWTHORNE, Z. MAO, D. HAHN, N. R. CROSS, G. BUCCI, T. ROY, M. A. WORSLEY, AND X. (RAYNE) ZHENG, *Ultra-thick three-dimensional interpenetrating graphene electrode architectures for high volumetric density energy storage*, Materials Horizons, (2026), pp. –, <https://doi.org/10.1039/D5MH01991E>.

[59] A. J. WATHEN, *Preconditioning*, Acta Numerica, 24 (2015), pp. 329–376, <https://doi.org/10.1017/S0962492915000021>.

[60] P. J. WEDDLE, T. LI, D. B. SULAS-KERN, R. J. TANCIN, N. DUNLAP, B. J. T. DE VILLERS, K. M. WIADEREK, A. M. COLCLASURE, AND D. P. FINEGAN, *Depth-resolved lithiated gradients in pristine and laser-ablated anodes during fast charging*, Journal of The Electrochemical Society, 172 (2025), p. 090515, <https://doi.org/10.1149/1945-7111/ae01e0>.

[61] F. WIESNER, A. LIMPER, C. MARTH, A. BRODERSEN, M. WESSLING, AND J. LINKHORST, *Additive manufacturing of intertwined electrode pairs-guided mass transport with gyroids*, Advanced Engineering Materials, 25 (2023), p. 2200986, <https://doi.org/10.1002/adem.202200986>.

[62] J. WU, V. SRINIVASAN, J. XU, AND C. WANG, *Newton-Krylov-multigrid algorithms for battery simulation*, Journal of the electrochemical society, 149 (2002), p. A1342, <https://doi.org/10.1149/1.1505635>.

[63] S. XU AND L. CAO, *Optimal convergence in finite element semidiscrete error analysis of the Doyle–Fuller–Newman model beyond one dimension with a novel projection operator*, IMA Journal of Numerical Analysis, (2025), p. draf065, <https://doi.org/10.1093/imanum/draf065>.

[64] X. XUE, S. CHANDRASEKARAN, C. ZHU, M. A. WORSLEY, AND Y. LI, *Architecting the third dimension of electrochemical energy storage*, ACS Energy Letters, (2026), <https://doi.org/10.1021/acsenergylett.5c03653>.

[65] X. XUE, L. FENG, Q. REN, C. TRAN, S. EISENBERG, A. PINONGCOS, L. VALDOVINOS, C. HSIEH, T. W. HEO, M. A. WORSLEY, C. ZHU, AND Y. LI, *Interpenetrated structures for enhancing ion diffusion kinetics in electrochemical energy storage devices*, Nano-Micro Letters, 16 (2024), p. 255.

[66] B. YAN, C. LIM, L. YIN, AND L. ZHU, *Three dimensional simulation of galvanostatic discharge of LiCoO<sub>2</sub> cathode based on X-ray nano-CT images*, Journal of The Electrochemical Society, 159 (2012), p. A1604, <https://doi.org/10.1149/2.024210jes>.

[67] F. ZHANG, M. WEI, V. V. VISWANATHAN, B. SWART, Y. SHAO, G. WU, AND C. ZHOU, *3D printing technologies for electrochemical energy storage*, Nano energy, 40 (2017), pp. 418–431, <https://doi.org/10.1016/j.nanoen.2017.08.037>.